The Effect of Humpback Whale-like Leading Edge Protuberances on Hydrofoil Performance

By

Derrick Custodio

A Thesis

Submitted to the Faculty

of the

WORCESTER POLYTECHNIC INSTITUTE

in partial fulfillment of the requirements for the

Degree of Master of Science

In

Mechanical Engineering

By

_____

December 2007

APPROVED:

_____

Dr. Hamid Johari, Advisor

_____

Dr. John J. Blandino, Committee Member

_____

Dr. David J. Olinger, Committee Member

_____

Dr. Charles W. Henoch, Committee Member

_____

Dr. Mark W. Richman, Graduate Committee Representative

Abstract

Despite its size the humpback whale is extremely maneuverable. This has been attributed to their use of pectoral flippers, along which protuberances are present along the leading edge. There has been speculation that the protuberances along the leading edge of the pectoral flipper act as a form of passive flow control. To examine the effects of protuberances on hydrofoil performance, the lift, drag, and pitching moments of two-dimensional hydrofoils with leading edge sinusoidal protuberances were measured in a water tunnel and compared to those of a baseline NACA 63_4-021 hydrofoil. The amplitude of the protuberances ranged from 2.5% to 12% of the mean chord length and the spanwise wavelengths were 25% and 50% of the mean chord length. This corresponds to the morphology found on the leading edge of humpback whale's flippers. Flow visualization using tufts and dye was also performed to examine the near surface flow patterns surrounding the hydrofoils. At angles of attack lower than the stall angle of the baseline the modified foils revealed reduced lift and increased drag. However, above this angle the lift generated by the modified foils was up to 50% greater than the baseline foil with little or no drag penalty. The amplitude of the protuberances has a large effect on the performance of the hydrofoils whereas the wavelength has little. Corroborating lift and drag measurements, visualizations show attached flow on the peaks of the protuberances and separation in the valleys at angles beyond the stall angle of the baseline foil.

Table of Contents

Nomenclature

c	=	length of chord
s	=	length of span
α	=	angle of attack
L	=	lift force
D	=	drag force
M	=	pitching moment
ρ_∞	=	freestream density
U_∞	=	freestream velocity
C_L	=	lift coefficient
C_D	=	drag coefficient
C_M	=	pitching moment coefficient
$\mathrm{Re_c}$	=	Reynolds number with respect to chord length
4S	=	hydrofoil with wavelength of 0.050 c, and amplitude of 0.025 c
4M	=	hydrofoil with wavelength of 0.050 c, and amplitude of 0.050 c
4L	=	hydrofoil with wavelength of 0.050 c, and amplitude of 0.120 c
8S	=	hydrofoil with wavelength of 0.250 c, and amplitude of 0.025 c
8M	=	hydrofoil with wavelength of 0.250 c, and amplitude of 0.050 c
8L	=	hydrofoil with wavelength of 0.250 c, and amplitude of 0.120 c

1 Introduction

1.1 Background

The idea of changing the leading edge of hydrofoils to resemble the leading edge of the humpback whale flipper was inspired by prior work of marine biologists who studied the morphology of the humpback whales pectoral flippers. Despite its enormous size (adults ranging from 12-16 m) and rigid body, the humpback whale is quite maneuverable compared to other species of whale. This is true especially during the whale's pursuit of prey. It has been determined by biologists such as Fish[1,2] through qualitative visualization of the humpback whale in nature that it can be said that the humpback whale has superior maneuverability in terms of turning radii and its movement through water relative to aquatic animals of comparable size. This maneuverability has been attributed to the use of their pectoral flippers[1,2]. A typical humpback whale flipper can be seen in Figure 1.

Figure 1: Humpback Whale flipper. Protuberances located on leading edge. Images from William W. Rossiter, Cetacean Society International and sciencenews.org

Fish and Battle report that humpback whale flippers have large aspect ratios ($s/c \approx 6$) as well as large scale protuberances located along the leading edge[1]. There is speculation that the protuberances act as a form of passive flow control. For the most part the humpback whale flipper has a symmetric profile shown in Figure 2**,** with a round leading edge and a sharp trailing edge. The thickness ratio (maximum cross-sectional thickness/chord length) of the flipper ranges from 0.20 to 0.28 of the chord length, with an average of 0.23 *c* and thickness ratio decreasing from mid-span to tip. The point of maximum thickness ratio varies from 0.20 *c* to 0.40 *c*. The cross-section of the flipper has a profile similar to the NACA 63_4-021, which is the hydrofoil profile that was used for baseline measurements throughout this report[1]. A comparison between the humpback whale flipper cross-sections and the NACA 63_4-021 airfoil profile can be seen in Figure 2**.**

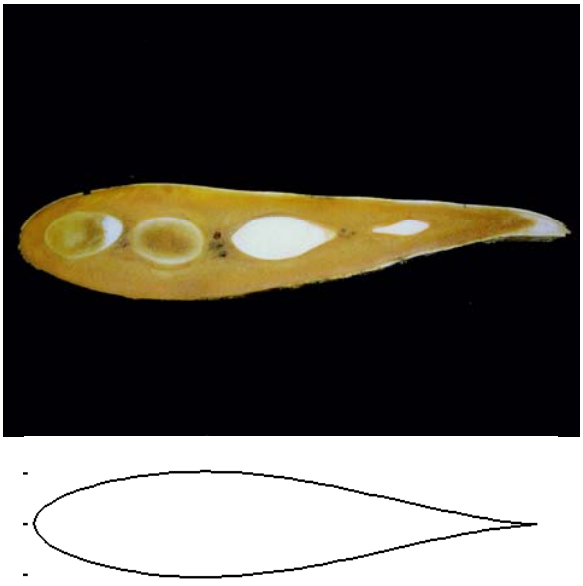

Figure 2: Comparison of a humpback whale pectoral flipper cross-section with the NACA 63_4-021 profile[1].

The protuberances found along the leading edge of the humpback flipper vary in amplitude and wavelength with span. The amplitude of the protuberances range from 2.5 to 12% of the chord length and the wavelength varies from 10 to 50% of the chord. It has been hypothesized that the protuberances act as a form of passive flow control[1] and/or a form of drag reduction[3].

An examination of the effects of leading edge protuberances on the load characteristics of a low aspect ratio wing using numerical methods was performed by Watts and Fish[4]. This study resulted in the determination that at an angle of attack of α = 10°, a 4.8% increase in lift was generated by a wing with protuberances over a baseline wing without protuberances. Afterward, a study of the load characteristics of a humpback whale flipper model in a wind tunnel was done by Miklosovic et al.[5]**.** Their findings can be seen in Figure 3**.** The models tested were similar in shape (tapering from root to tip) and aspect ratio to the actual humpback whale flipper. In general, the shape of the flipper models was the same, except that one of the models had protuberances along the leading edge and the other model, which acted as the baseline for comparisons, did not. Miklosovic et al. reported a 6% increase in maximum lift over the baseline wing and a 40% increase in stall angle by the flipper model with protuberances. Miklosovic's results also show that over the range of $10° \leq \alpha \leq 18°$ there is an overall decrease in drag when protuberances are present along the leading edge. Excluding the range of angle of attack $10° \leq \alpha \leq 12°$, Miklosovic et al. showed that higher lift to drag ratios are achieved when protuberances are present. This implies that protuberances, in essence, create a more efficient wing over certain angles of attack. Specifically, the post-stall angles of attack of

the baseline model, show significant increases in lift to drag ratio. Another study by Stein and Murray reported that a two-dimensional airfoil with protuberances equal in amplitude and wavelength equal to the average amplitude and wavelength of the humpback whale flipper results in a significant loss in lift and a large increase in drag[6]. Their measurements, however, were done at angles of attack ranging from 8° to 12°. However, no data past 12° was reported[6]**.** The difference between Stein and Murray's experiment[6] and the others is that Stein and Murray tested two-dimensional airfoils whereas the others tested finite wings. It is possible that the presence of protuberances on finite wings may have affected the spanwise flow over the wings. The effects of adding leading edge sweep on humpback whale flipper models with protuberances have also been investigated by Murray et al.[7]**,** They reported an enhanced aerodynamic performance with increasing sweep angle.

The addition of three-dimensional disturbances on two-dimensional bluff bodies has long been known to alter the regular vortex shedding and drag characterisitics[8-13] over the bodies. The drag reduction associated with the three-dimensionality stems from the resulting waviness of the separation line. For the foils considered in this study, the introduction of protuberances on the leading edge altered the entire flow field over the foil, and was expected to have different effects then the previously observed drag reductions.

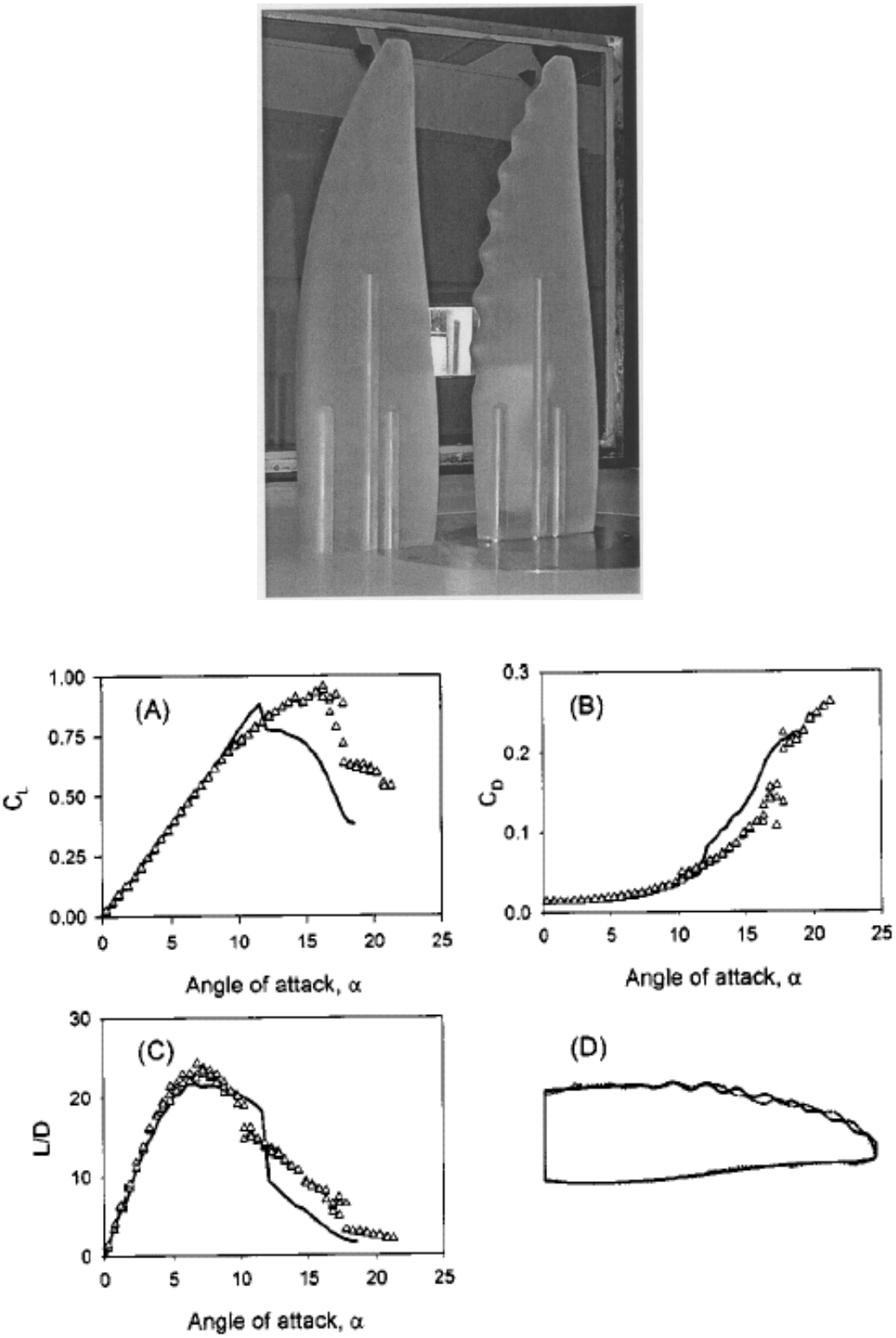

Figure 3: Top: Flipper models tested by Miklosovic[7]. Bottom: a) Lift coefficient vs. angle of attack b) Drag coefficient vs. angle of attack c) Lift to drag ratio vs. angle of attack d) Showing flipper model design.

Watts and Fish hypothesized that the protuberances along the leading edge of the humpback whale flipper act as some kind of passive flow control mechanism[4]. Flow control can be categorized into passive and active control schemes. Passive flow control can be described by non-moving parts that help create beneficial characteristics by a flow field surrounding an object. For example, stationary vortex generators (a passive flow control scheme) are essentially tabs that protrude from the surface of a wing into the boundary layer of fluid surrounding the wing[14]. Vortex generators create a vortex that brings high momentum fluid from outside the boundary layer back down to the surface of the wing. Passive flow control schemes are simple and contain no moving parts, but it is possible that detrimental effects such as increased drag can be caused by having a non-moving part in the flow field. Flow control can also be achieved through the use of active mechanisms. Whereas passive flow control consists of systems of non-moving parts capable of controlling fluid flow, active systems are made up of mechanisms which are not stationary, but are activated by and can be mechanically manipulated. Active mechanisms are useful because they are capable of being activated at specific times. Therefore flow control can be achieved when need be, therefore presumably eliminating the detrimental effects such as the added drag of having a flow control mechanism always within the flow field. An example of active flow control would be mechanically actuated vortex generators. However, there is usually the added complexity associated with active systems. It is possible that protuberances along a wings leading edge can be useful in both a passive or active flow control scheme.

1.2 Application

Virtually any control surface, as well as some propulsion systems, could potentially benefit from protuberances as a form of flow control. Most control surfaces and propulsion systems are lifting surfaces with a hydrofoil/airfoil profile, which are capable of imparting fluid momentum change, and hence creating force on the surface itself. Normally, flow attachment and lift and drag considerations inhibit the capabilities of the control surface. Any type of enhancement of the control surface authority and aerodynamic characteristics or range of operation could be useful.

It is possible that leading edge protuberances could be used as an advantageous mechanism employed by a control surface so long as the beneficial effects are not overshadowed by the detrimental effects. Control surfaces which operate at high angles of attack such as boat rudders, torpedo and missile fins, as well as military aircraft wings and stabilizers could potentially benefit from leading edge protuberances. Leading edge protuberances could increase performance at high angles of attack on these mechanisms as well as increase the range of operation of the control surface. A deformable control surface could also benefit immensely from leading edge protuberances. For example, an active leading edge that deploys protuberances at high angle of attack could take advantage of added lift at high angles of attack without any detrimental effects.

Propulsion systems could also benefit from leading edge protuberances. In the field of bio-mimetic propulsion, which can be described as forms of propulsion that imitate life, such as a seal propelling itself through water, or a bird using its wings to propel itself through the air, may benefit by implementing protuberances on the lifting and propulsive surfaces. Also, propellers are a very popular form of propulsion, as they

are used to propel almost all boats and some airplanes. It is possible that the flow characteristics caused by leading edge protuberances could potentially benefit these forms of propulsion as well.

1.3 Objectives

Most prior approaches associated with leading edge protuberances examined wings of finite span or two dimensional foils over small ranges in angle of attack. The experiments reported here contain the objective of excluding parameters such as finite span and tip effects, etc. Because previous work on the effects of protuberances focused on finite wings over small ranges of angle of attack, it was necessary to examine the effect of uniform spanwise protuberances on the performance of 2-D hydrofoils over a broad range of angle of attack. This study reported here ruled out parameters inherent in finite wings to simplify the situation and test only the effects of protuberances. Also, at the current time there is no previous work examining the effect that different protuberance sizes (amplitude and wavelength) have on hydrofoil characteristics. Therefore protuberances were varied in a number of ways. This way, not only are the effects of protuberances in general compared to the baseline foil, but the effect caused by the type of protuberance is examined as well. Two-dimensional foils were created with uniform tubercles along the leading edge span, but with varying wavelength and amplitude between foils, and were tested in the Naval Undersea Warfare Center (NUWC) water tunnel in Newport, RI. Two different wavelengths and three amplitudes were tested to examine the effect of the protuberance size. The main objectives of this study are as follows:

- To examine the effects of leading edge deformations similar to the humpback whale flippers leading edge on the lift, drag, and stall characteristics of 2-D hydrofoils over a wide range of angles of attack.
- To examine the effects of protuberances on the flow field over hydrofoil surfaces.

- To understand the causes for any performance enhancements.

To examine the hydrodynamic characteristics of the hydrofoils, load measurements were carried out on the foils; detailed examination of the flow field surrounding the foils using flow visualization techniques were also conducted.

2 Experimental Setup

2.1 Hydrofoil Sections

Two sets of hydrofoils along with one other hydrofoil were machined and anodized for the experiments. Pro-Engineer, a computer-aided design (CAD) program was used to design the models; the hydrofoils were fabricated out of aluminum stock in WPI's Washburn shops using a 3-axis computer numerical code (CNC) machine. Because of the differences in leading edge geometry between the baseline hydrofoil and hydrofoils with protuberances it was necessary to develop a way to ensure that the planform areas of all of the hydrofoils were the same. To do this, the leading edge geometry and trailing edge geometry on foils with protuberances were designed separately and combined subsequently. To create the leading edge geometry on foils with protuberances a sine wave of certain wavelength and amplitude (dependant on the hydrofoil being created) was generated at the leading edge of the hydrofoils with the inflection points being equal to the baseline leading edge. The trailing edge section of the hydrofoils was kept the same throughout all hydrofoil models including the baseline. To connect the leading edge and trailing edge geometries a point of tangency was chosen where the two sections could be combined. This point of tangency was three times the amplitude of the protuberances of the hydrofoil. To generate the profile shape a curve was drawn between the inflection points of the protuberances to the point of tangency which was equal to the baseline leading edge shape. To generate the remainder of the leading edge section, the baseline leading edge shape was essentially stretched and compressed filling in the rest of the section according to the leading edge sine wave. The hydrofoils were anodized in matte black in order to aid in visual contrast for flow

visualization experiments. The hydrofoils were based on the NACA 63_4-021 airfoil profile. This profile was chosen because the thickness ratio and general profile shape are similar to the actual cross-sectional profile of the humpback whale flipper.

The first set of seven hydrofoils, shown in Figure 4, was used for load measurements; the foils in this set had a mean chord length of $c = 102$ mm and a span of $s = 203$ mm, therefore all of the hydrofoils in the set had the same planform area. One hydrofoil, which had a straight, protuberance-free, leading edge, was used as a baseline. The other six hydrofoil geometries in the set had spanwise sinusoidal protuberances along the leading edge. The leading edge geometries were defined by the amplitude and wavelength of the protuberances. Three amplitudes of 0.025 *c*, 0.050 *c*, and 0.120 *c*, and two wavelengths of 0.250 *c*, and 0.500 *c* were used to define the size of the protuberances. To aid understanding, the nomenclature used throughout the rest of the report describing the leading edge geometries is as follows; 8 and 4 represent wavelengths of 0.250 *c*, and 0.500 *c*, respectively, and S (small), M (medium), and L (large) represent amplitudes of 0.025 *c*, 0.050 *c*, and 0.120 *c*, respectively. These parameters fall within the range of the protuberances found on the humpback whale in nature.

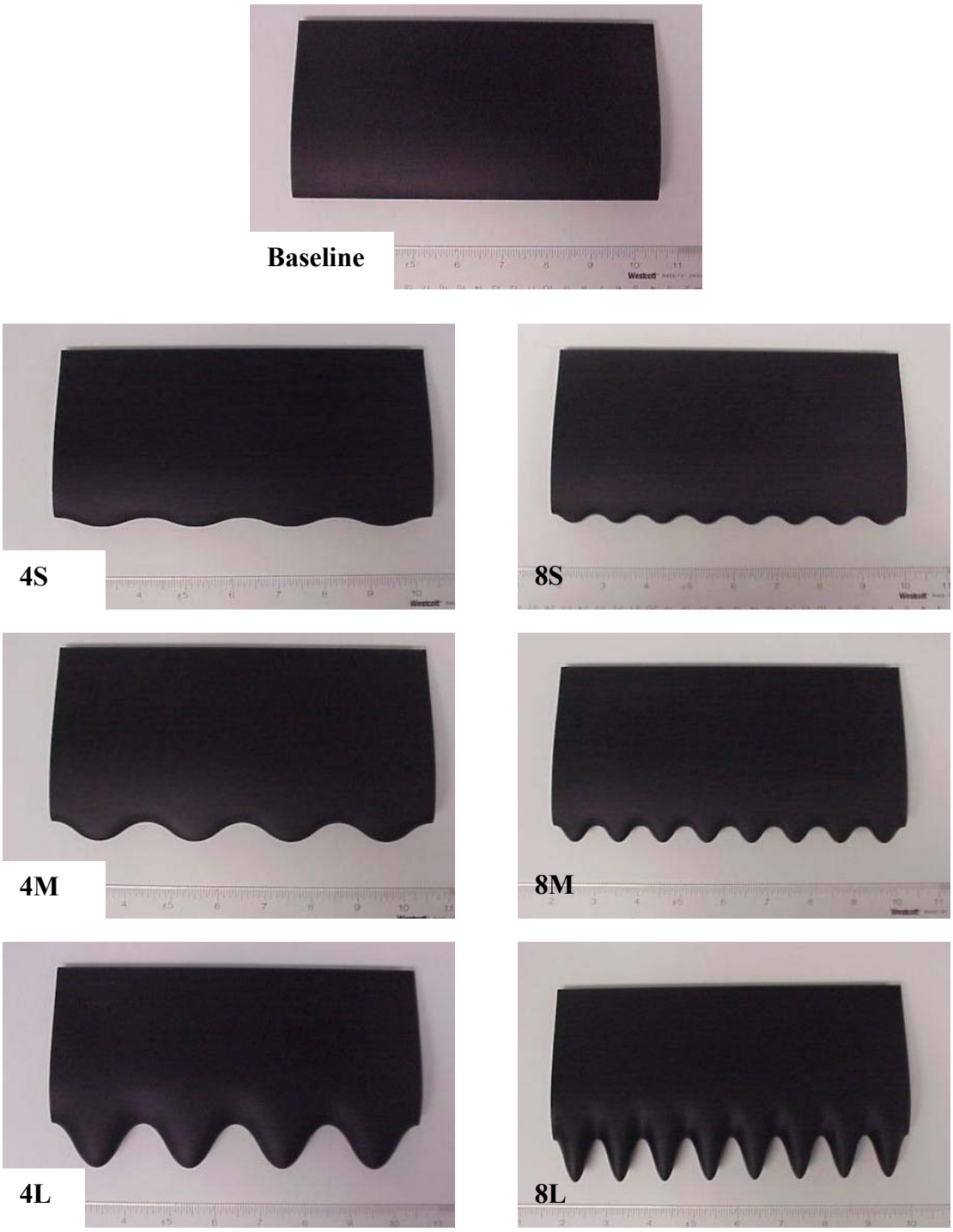

Figure 4: First set of hydrofoils. Wavelength nomenclature; 4 = 0.050 *c*, 8 = 0.025 *c*. Amplitude nomenclature; S = 0.025 *c*, M = 0.050 *c*, L = 0.120 *c*.

The second set of hydrofoils, shown in Figure 5, was used in flow visualization experiments. Again, this set of hydrofoils had a mean chord length of $c = 102$ mm, but

with a span of $s = 305$ mm; this set spanned the entire height of the water tunnel test section. The second set consisted of four hydrofoils containing a baseline, and three hydrofoils with 4L, 4M, and 8M leading edge protuberance geometries. Attached to the low pressure side of these hydrofoils were tufts, made of flexible, yellow yarn that was 0.23 mm in diameter and were used to visualize the flow patterns of water over this side the hydrofoil surface. The flow patterns were captured using still photography and video recording.

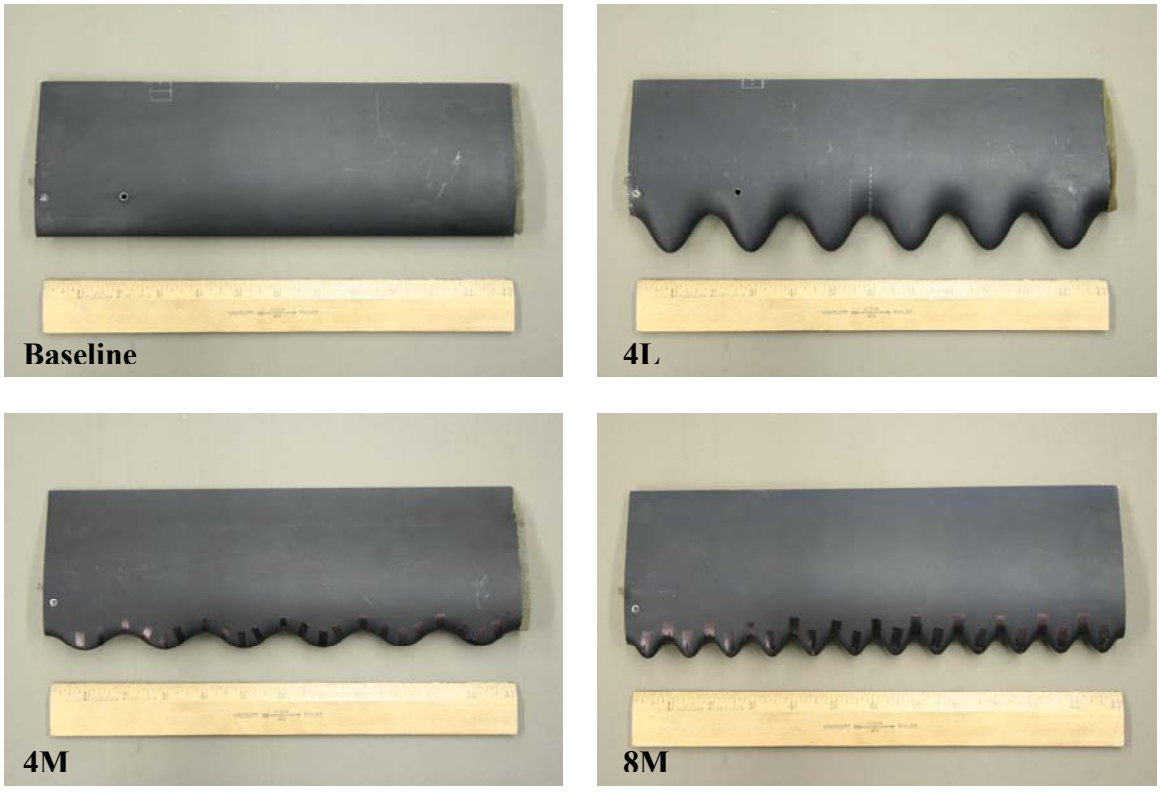

Figure 5: Second set of hydrofoils with 305 mm span.

A final hydrofoil, 8M*, shown in Figure 6**,** was also fabricated and was used for load measurements. The dimensions of the hydrofoil were similar to the first set, its span being $s = 203$ mm, but its mean chord length was $c = 104.5$ mm. Its leading edge geometry consisted of a wavelength = 0.250 *c*, and an amplitude = 0.050 *c*. Therefore, the planform area of this hydrofoil was larger than the first set of hydrofoils. Since the average chord length of the 8M* foil was longer then the 8M foil, the leading edge radius was necessarily smaller on the 8M* foil than the 8M foil at any given spanwise position (this can be seen in Figure 7). The purpose of this foil was to see the effect of, in essence, adding the protuberances to the leading edge of the baseline hydrofoil, shown in Figure 7. The first set of hydrofoils had the same planform area, implying that in order to create the leading edge geometries, the sinusoidal protuberances were through the baseline, peaks extending beyond the baseline, and valleys going inward. In the case of an active flow control mechanism it is considered an easier task to employ the protuberances that are moved outward rather than outward and inward from a baseline shape.

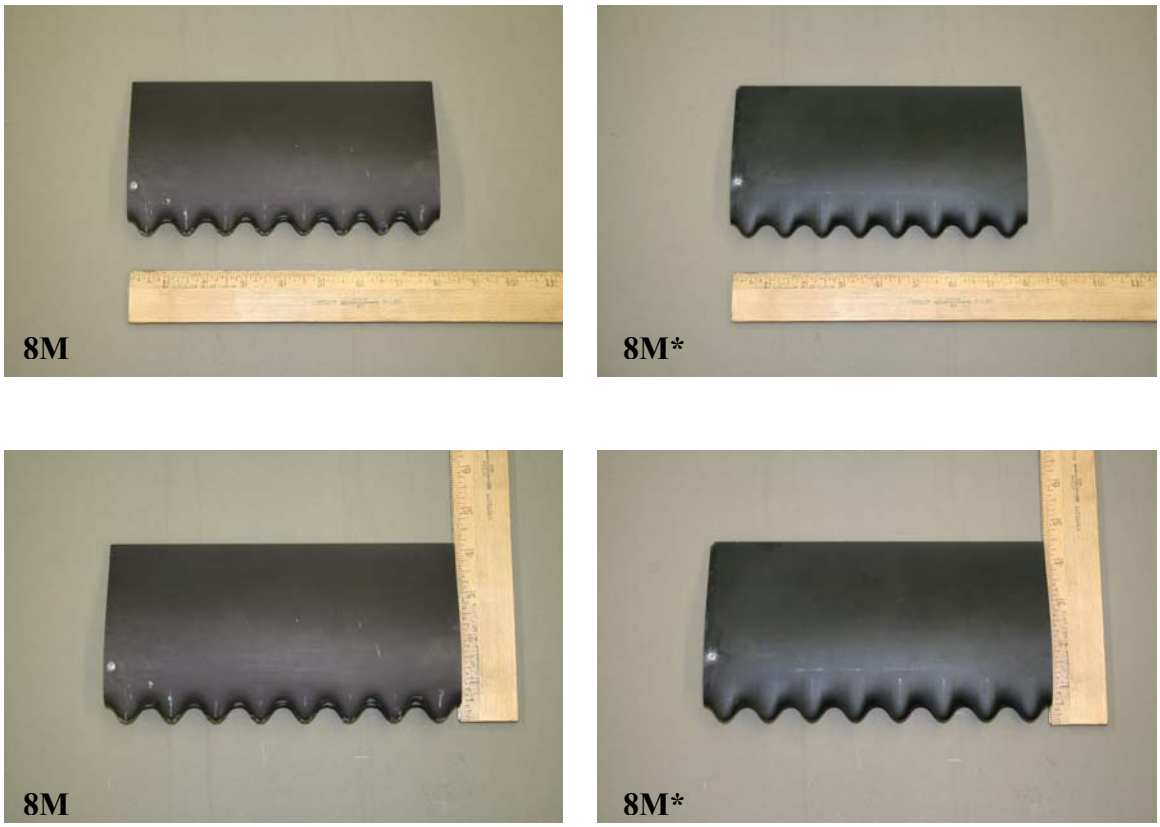

Figure 6: 8M and modified 8M foils

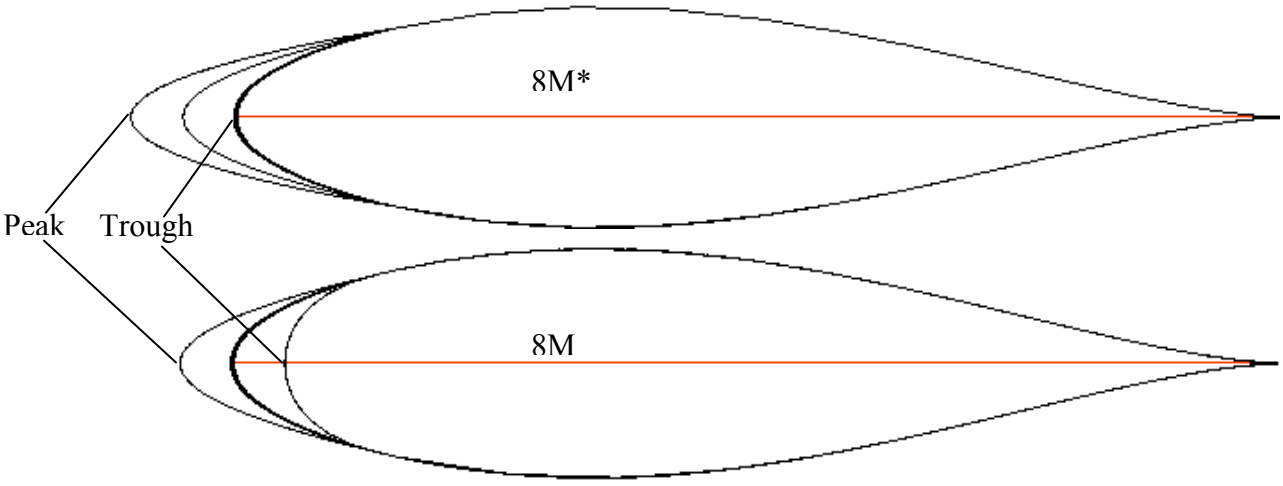

Figure 7: Profile comparison between 8M and 8M* foil.

2.2 Water Tunnel

The experiments were conducted in the Naval Undersea Warfare Center (NUWC) water tunnel in Newport, RI shown in Figure 8. The water tunnel is capable of sustaining velocities up to 10 m/s, and has 0.30 m square test section and is capable of retaining a turbulence level of less than 2%, with uniform (i.e. constant) freestream flow in a 6"×6" square in the center of the tunnel test section. To achieve the correct testing speeds it was necessary to calibrate the water tunnel impeller RPM to the freestream velocity inside the tunnel. This is because blockage effects cause changes in the freestream speed. When some of the tunnel's test section cross sectional area is taken up by an object, fluid will speed up between the sides of the tunnel and the the object. Since blockage must be accounted for in a closed water tunnel, the impeller RPM necessary to sustain a speed of 1.8 m/s was determined as a function of angle of attack. The freestream velocity was measured at a point $6.5\,c$ upstream of the hydrofoil using a fiber-optic Laser Doppler Velocimetry (LDV) system. All experiments reported were done at a freestream speed of 1.8 m/s, yielding a Reynolds number based on the freestream velocity and the hydrofoil chord length of $\mathrm{Re}_c = 1.83\times10^5$. The Reynolds number of the humpback whale flipper with respect to chord length is estimated to be around $\mathrm{Re}_c = 5\times10^5$. The experimental apparatus used for measuring forces was not capable of supporting loads at a Reynolds number of 5×10^5, therefore a lower Reynolds number was chosen for the force measurements reported. Reynolds number effects were considered negligible due to the turbulent nature of the flow over the hydrofoils.

A very accurate pitch-yaw mechanism, shown in Figure 9, was implemented to adjust the angle of attack from outside of the water tunnel. The hydrofoils spanned the water tunnel vertically and were connected to the pitch-yaw mechanism by means of a shaft which extended from outside of the test section through the mechanism and into the hydrofoil being within the test section.

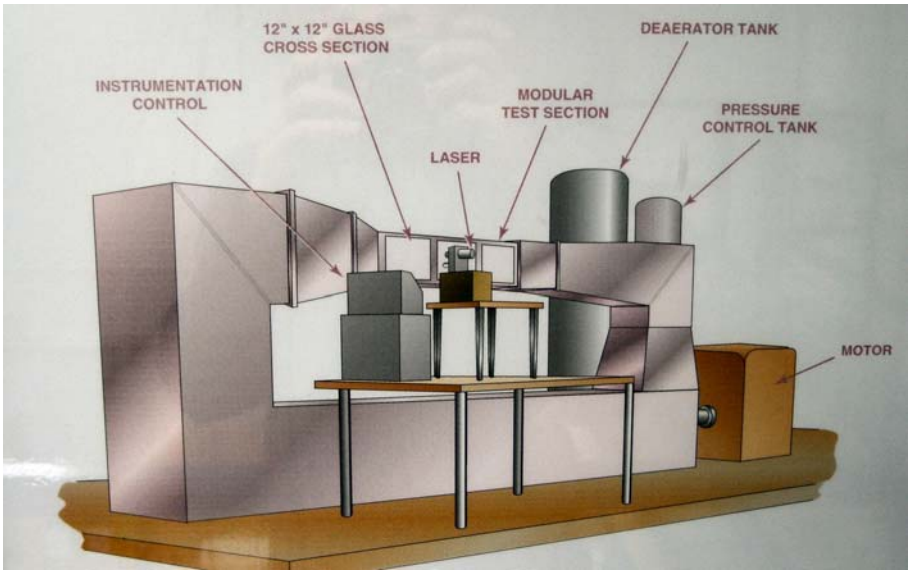

Figure 8: Schematic of the NUWC water tunnel.

2.3 Load Measurements

The lift and drag forces as well as the pitching moment on the 203 mm hydrofoils were measured using a strain gage 6-axis waterproof load cell. The hydrofoils were attached to the load cell at a point 0.25 c from the leading edge of the hydrofoils. The load cell extended 102 mm into the water tunnel, creating a gap between the lower surface of the water tunnel and the hydrofoil. To minimize 3-D effects it was necessary to incorporate a fence which could be attached to the bottom of the hydrofoil. The fence was made round because when the angle of attack was changed it was necessary to rotate the entire apparatus. The fence was in turn attached to the load cell. The load cell was implemented into the pitch-yaw mechanism which allowed the measurement of forces and moments at various angles of attack. The top of the hydrofoil was bounded by the ceiling of the water tunnel. The force measurement setup is shown in Figure 9. Force and moment measurements were taken at angles of attack ranging from $-6° \leq \alpha \leq 30°$. The measured forces were converted to lift, drag, and pitching moment coefficients using the freestream dynamic pressure and the planform area of the hydrofoils.

It was necessary to apply certain corrections to the load measurements to obtain accurate values for the lift, drag, and moment coefficients. Because there was a fence attached to the hydrofoils there was necessarily an additional drag contribution that needed to be taken into account. This was done by measuring the drag at on the fence alone at multiple angles of attack within the range that the experiments reported were conducted and subtracting the average of these values from the total drag measured on the hydrofoil-fence combination. By doing this the drag contribution of the fences is negated. The coefficients were also corrected for blockage effects in the form of solid and

wake blockage. Blockage affects the measured lift, drag, and moment values as well as the effective angle of attack. The dimensionless coefficients were corrected for blockage using the methods outlined by Pope and Ray[15].

The load cell in this experimental set-up has an uncertainty of 0.04 N for force measurements, and 0.001 N-m for the pitching moment. These values, along with uncertainties in the freestream velocity and hydrofoil dimensions amount to less than 1% of the total lift and drag measured, and 3% of the total pitching moment. The estimated uncertainty of the angle of attack is 0.2°. Load cell uncertainties will be discussed further in Section 2.5.1.

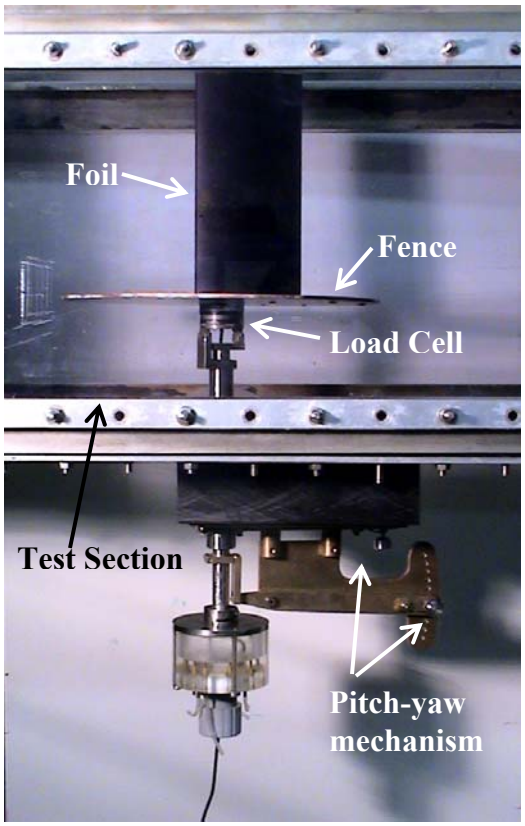

Figure 9: Force measurement setup.

2.4 Flow Visualization

2.4.1 Tufts

The second set of hydrofoils was used in flow visualization experiments. The hydrofoils in this set had a span of $s = 305$ mm, which spanned the entire tunnel height. The hydrofoils could be directly attached to the pitch-yaw mechanism by means of a shaft. The shaft was attached to the pitch-yaw mechanism and entered the water tunnel though the bottom of the test section and into the end of the hydrofoils. The shaft entered the hydrofoil 0.25 c from the leading edge of the hydrofoils.

Tufts attached to the low pressure side of hydrofoils were used to examine the near surface flow patterns that arose at different angles of attack at a freestream speed of 1.8 m/s. The tufts used were made of yellow nylon thread, and were 0.23 mm in diameter. The tufts were attached to the surface of the hydrofoils using Scotch brand invisible tape. They were spaced along the hydrofoil surface by a distance of 12.7 mm in the spanwise and streamwise directions. Also, the exposed tuft material was 12.7 mm long, implying that the rows of exposed pieces of tuft material ended where the next row of tufts began. The tufts were arranged in such a way that when flow was completely attached the ends of the exposed tufts would line up with the beginning of the tuft in the next row so that the entire chord length would be covered by exposed tufts. Also, tufts were attached to the hydrofoils along the leading edge of all of the hydrofoils of the set. Along the leading edge of the hydrofoils with protuberances, there was at least a tuft on the peak, valley, and inflection point of each protuberance. An example of a tufted foil can be seen in Figure 10.

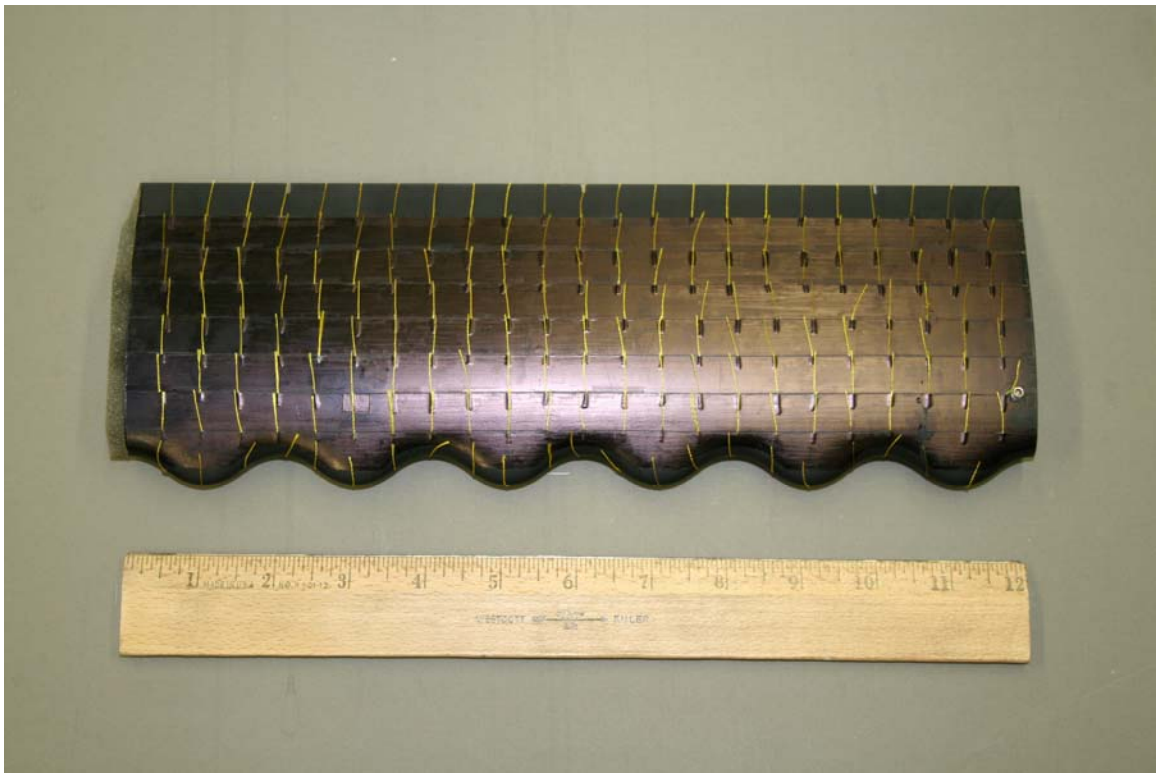

Figure 10: 4M foil with tufts.

The flow patterns were captured using still image photography, as well as video recording. The lighting used varied depending on whether still photography or video recording was being used. The camera used for still photography was Canon DS 126071 Digital Rebel XT. The lighting consisted of a gray background that was lit from the front by a floodlight reflecting its light off of the background back toward the camera lens. This created the effect of the hydrofoil being backlit. The reflected light created a clear contrast between the background and the hydrofoil. Also, 18" fluorescent lights were attached outside of the water tunnel test section both on the top and bottom of the test section. This aided in creating contrast between the yellow tufts and the black hydrofoil. Lastly, the front of the test section was lit using floodlights to light the front surface of the hydrofoil. The camera used was capable of automatic shutter speed and aperture

settings. It was necessary to use automatic settings for shutter speed and aperture because, depending on the angle of attack of the hydrofoil, the tufts were moving in erratic fashion, and therefore constantly reflecting different amounts of light back into the camera lens. The focus was manually set at the beginning of each set of pictures that was taken.

The flow patterns were also recorded using video photography. The camera used was a Sony DCR-HC96 Handycam. The video was backlit by a floodlight which shone through a blue cloth background. This created a dim, diffuse light, thus creating less of a contrast between the background and the hydrofoil than in the former case of still photography. This created the greatest contrast between the tufts and the background and hydrofoil surface. The other lighting elements remained the same as the setup used for still photograph. The camera light and focus settings were automatically set.

2.4.2 Dye Visualization

A second flow visualization experiment using dye was conducted on the 203 mm span foils to gain a qualitative understanding of the near surface flow field around the hydrofoils. It was carried out by injecting red dye into the interior of the hydrofoil and out through holes or ports in the leading edge of the 4L hydrofoil and also through the baseline hydrofoil for comparison. The freestream velocity for these experiments was 0.015 m/s to allow detailed examination of the flow field at high angles of attack. At higher freestream velocities, the dye would break up and diffuse rapidly, thereby eliminating the beneficial aspects of dye flow as a visualization tool.

To flood the inside of the hydrofoil with dye, it was necessary to create a 9.25 mm hole in the quarter chord point of the hydrofoils from one end of the span to the other. To create a dye flow from the inside of the hydrofoil to the leading edge, holes of 1.3 mm diameter were fashioned that extended from the leading edge surface to the inner orifice spanning the hydrofoil length. The ports through which the dye would flow were located at every protuberance peak, valley, and inflection point, except at the ends of the hydrofoil. Correspondingly, the ports along the leading edge of the baseline foil were created 12.5 mm apart.

A pressurized tank outside of the water tunnel was used to force dye into the hydrofoil and finally out through the holes in the leading edge. The tank would pressurize a container filled with the red dye, which would in turn force the dye through a tube towards a valve. The valve was capable of minute adjustments of dye flow. After the dye left the valve, it would pass through the hydrofoil and be released into the water through the leading edge of the hydrofoil. This configuration can be seen in Figure 11.

To eliminate spanwise flow and tip vortices at the ends of the hydrofoils, fences were incorporated into the setup at each end of the hydrofoils. The same pitch-yaw mechanism used in the tuft visualization experiments was used in the dye experiments to adjust the angle of attack of the hydrofoils.

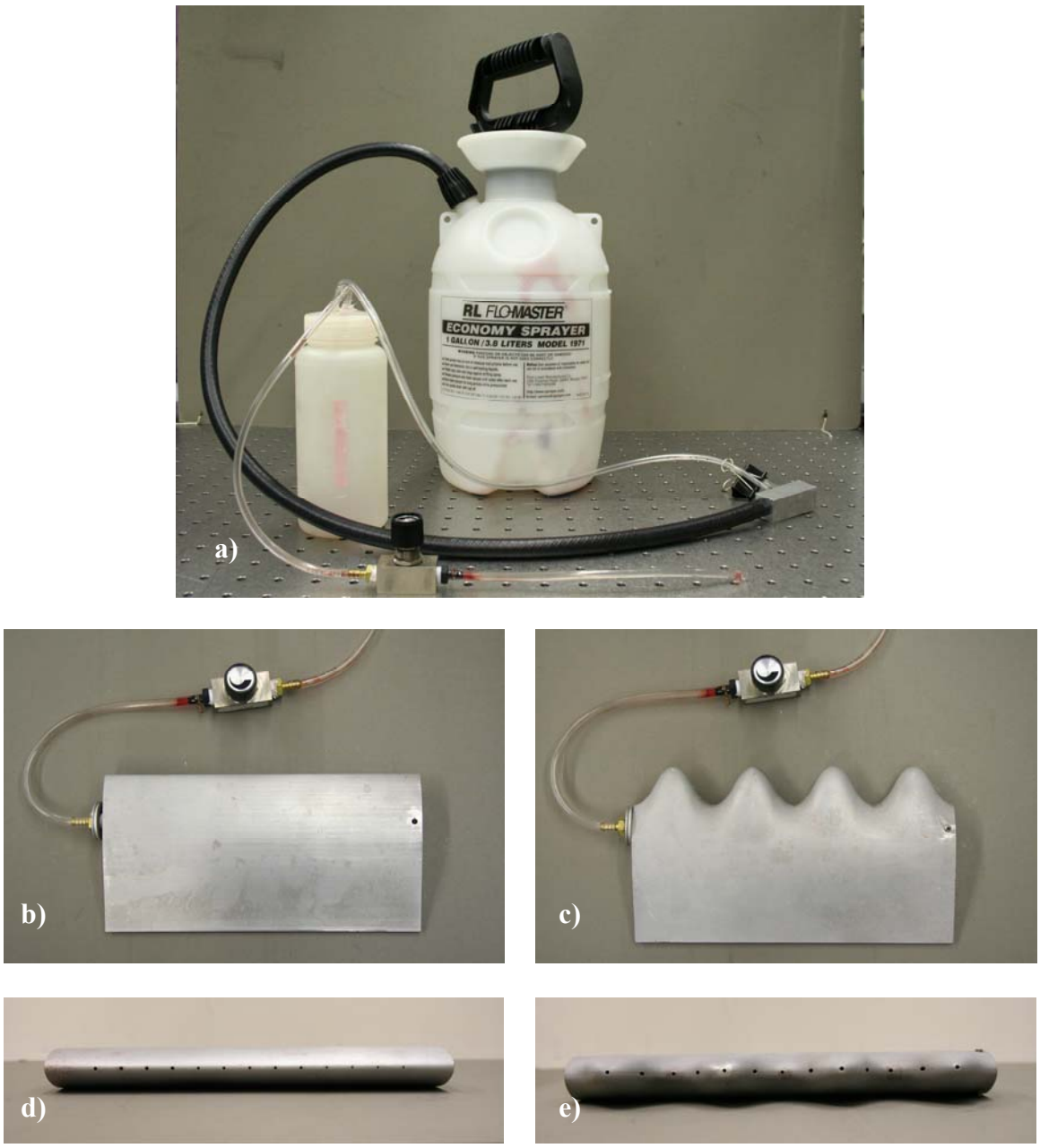

Figure 11: a) Dye injection system; b) dye valve connected to baseline foil; c) dye valve connected to 4L foil; d) leading edge of baseline foil with dye ports; e) leading edge of 4L foil with dye ports.

2.5 Uncertainty Quantification

The measurement techniques used to carry out the experiments documented in this report necessarily carry along some uncertainty. The force measurements also contain some level of uncertainty in the measured values. Sources of uncertainty are discussed below.

2.5.1 Uncertainty of Measurement Techniques and Devices

Sources of uncertainty can be found in several places. When measuring forces on the hydrofoils, there is uncertainty in the load cell voltage output, which translates into a force uncertainty of ± 0.04 N and moment uncertainty of 0.001 N-m. Also, the pitch-yaw mechanism used to adjust the angle of attack of the hydrofoils possesses some uncertainty because it is adjusted manually and the true value is not known exactly how true the value of the angle is. However, it is possible to make an estimate of the largest possible error that could be made on any one adjustment of angle. In the experiments outlined previously, the uncertainty estimate of the pitch-yaw mechanism can be estimated at ± 0.2°. The water tunnel freestream speed also has some uncertainty associated with it. The value of the uncertainty associated with the freestream tunnel velocity is 0.5% of the expected velocity. For example, the load measurements and tuft visualization experiments were conducted at a speed of 1.8 m/s, which correlates to a tunnel velocity uncertainty of ±.009 m/s.

The hydrofoils used in the experiments also yield some uncertainty in final measurements. Although the foils were CNC machined, the foils are slightly different than the ideal drawings. This deviation is not just caused by possible machining error;

user error also has an effect. For example, when machining a slight mistake may be made by the user in the orientation of the piece. Not only, is there possible human error in fabricating a piece but there is a small amount of uncertainty in the machining process itself. These possibilities create a need for detailed examination of the part once finished. After the hydrofoils were fabricated, chord measurements were taken on the foils at different places along the span, and the error caused by machining and user error resulted in no more than a 0.8% difference from the expected chord length value of the foil.

With the known sources of error and their values it is possible to determine an overall error or uncertainty in the load measurements at any given angle of attack that was tested. Using the methods outlined by Coleman and Steele[16], the following ranges of uncertainty were determined on the baseline foil: a) $0.86\% \leq \text{Uncertainty}_{C_L} \leq 3.9\%$ error in C_L over the range of C_L measured, b) $0.8\% \leq \text{Uncertainty}_{C_D} \leq 7.1\%$ error in C_D over the range of C_D measured, c) $0.86\% \leq \text{Uncertainty}_{C_M} \leq 12.5\%$ error in C_M over the range of C_M measured, and d) $\text{Uncertainty}_{\alpha} \approx .67\%$ for maximum $\alpha \approx 30°$.

3 Results

3.1 Force Measurements

3.1.1 Baseline Hydrofoil

The time averaged lift, drag, and pitching moment forces experienced by the hydrofoils were determined as a function of angle of attack. These aerodynamic characteristics can provide a measure of the hydrofoil performance. Dimensionless coefficients will be used throughout the report in the form of the lift, drag and moment coefficients to describe these forces and are calculated in the following way (tunnel blockage effects are taken into account prior to final calculation):

Lift coefficient:

$$C_L = \frac{L}{\frac{1}{2}\rho_\infty U_\infty{}^2 cs}$$

Drag coefficient:

$$C_D = \frac{D}{\frac{1}{2}\rho_\infty U_\infty{}^2 cs}$$

Pitching moment coefficient:

$$C_M = \frac{M}{\frac{1}{2}\rho_\infty U_\infty{}^2 cs}$$

The baseline lift coefficient (C_L) is shown in Figure 12a as a function of α. The baseline lift coefficient behaves as expected, with the lift increasing at a linear rate with α until $\alpha \approx 11°$, and continuing afterwards but at a lower rate. The slope of the linear portion is shown in Table 1 as $dC_L/d\,\alpha$. As α is increased past 11°, C_L continues increasing but at a reduced rate until $\alpha \approx 21°$. This is an indication of flow separation, which occurs when

the boundary layer on an object encounters a large enough adverse pressure gradient capable of reversing the flow. Separation results in decreased lift generated by the object as well as increased drag, and can be seen in Figure 12a at $11° \leq \alpha \leq 21°$. Beginning at the trailing edge, flow separation can also be seen qualitatively in Figure 26 as tufts pointing in the upstream direction. As the angle of attack is increased, separation increases as well, creeping towards the leading edge. At $\alpha \approx 21°$ the foil is completely stalled. Stall occurs when the flow has separated along the entire low pressure side of the foil including the leading edge and results in catastrophic loss in lift and large increases in drag. The maximum C_L normally appears just prior to the stall angle and in this case happens to be $C_L \approx 1.13$. As α crosses the stall angle a dramatic loss of lift has occurred, and from $22° \leq \alpha \leq 28°$ the post-stall lift coefficient of the baseline foil is nearly constant with a value of $C_L = 0.57$.

The drag coefficient (C_D) of the baseline foil as a function of angle of attack can be seen in Figure 12b**.** The drag on the baseline foil theoretically has its lowest value at $\alpha = 0°$, when the projected area of the foil is at its lowest, and its maximum value at $\alpha = 30°$ when the projected area of the foil is largest. As the angle of attack is increased form $\alpha = 0°$, the C_D rises in a quadratic fashion. When α reaches an angle where separation is occurring, the drag begins to rise at a more rapid rate until it reaches the stall angle where there is a sharp discontinuity and drag suddenly increases dramatically. After the stall angle is crossed, drag on the foil continues to increase in quadratic fashion once again. The minimum value of the drag coefficient is ≈ 0.017 at an angle of $\alpha \approx 0°$, whereas the maximum value was ≈ 1.20 at an angle of 30°.

The pitching moment coefficient referenced to the ¼ *c* point (C_M) with respect to angle of attack is found in Figure 13a**.** The pitching moment is the moment generated when the lift force on an airfoil is at a location other than its aerodynamic center. When the lift force is applied at a place in front of or behind the aerodynamic center along the chord, a moment is created about this point causing a clockwise or counterclockwise pitch. The sign convention used in this report is determined in the following way: if the downstream direction is considered the positive *y* direction, then through the use of the right hand rule, pitching moment causes rotation about the *x*-axis. Using this rule, a clockwise moment about the *x*-axis yields a negative pitching moment, and a counterclockwise rotation yield a positive pitching moment. In Figure 13b, the baseline pitching moment coefficient is positive at negative angles of attack and goes negative with increasing angles of attack. This trend continues until the stall angle is reached and the moment drastically decreases. The lift, drag, and pitching moment characteristics described are all common to this type of foil profile and the observed trend in baseline foil matches closely with measurements taken by Abbott and Von Doenhoff on the same airfoil section[17] at Reynolds numbers of three and six million.

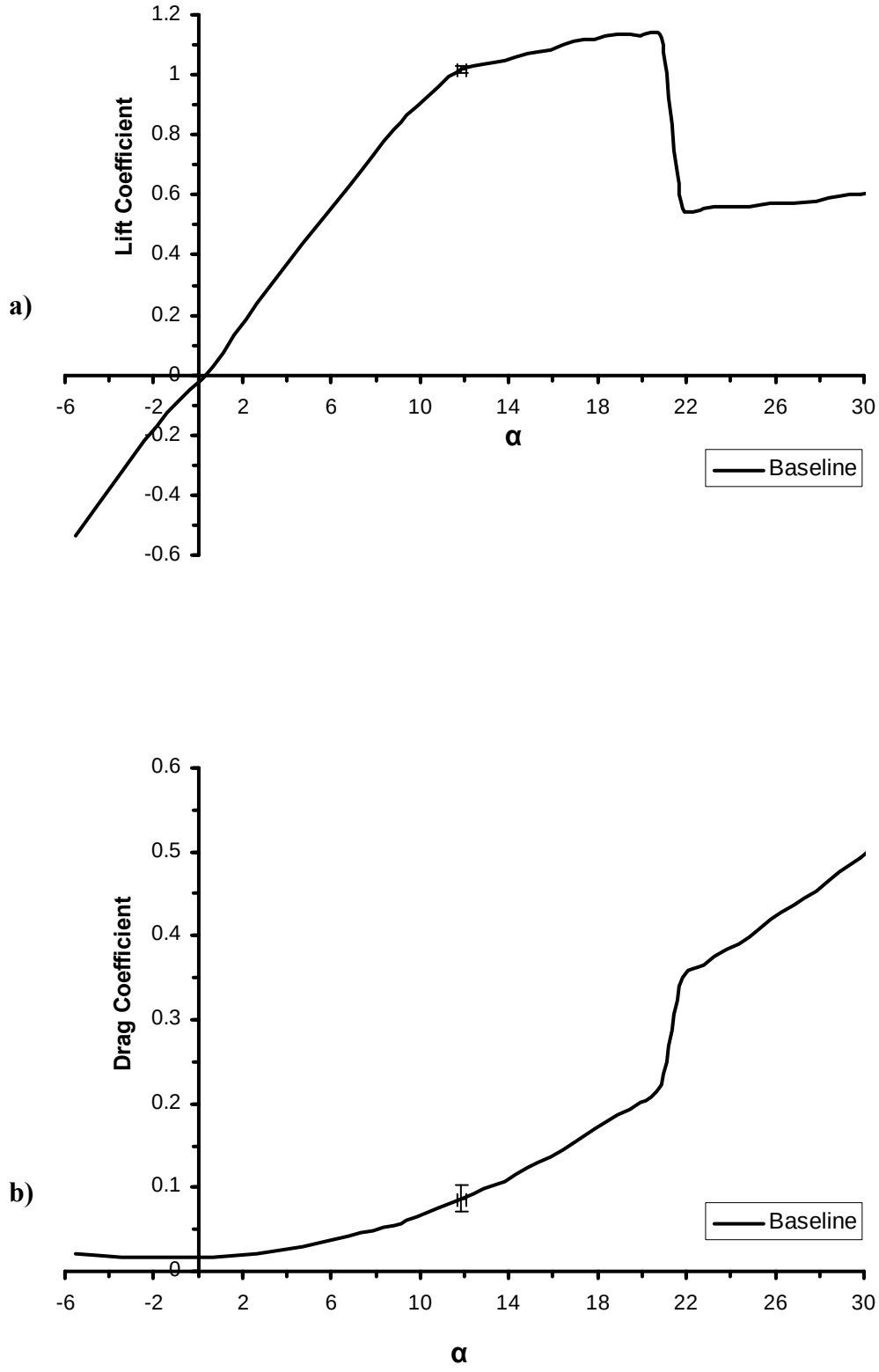

Figure 12: a) Lift and b) drag coefficient on baseline hydrofoil, with error bars in place at $\alpha \approx 12°$

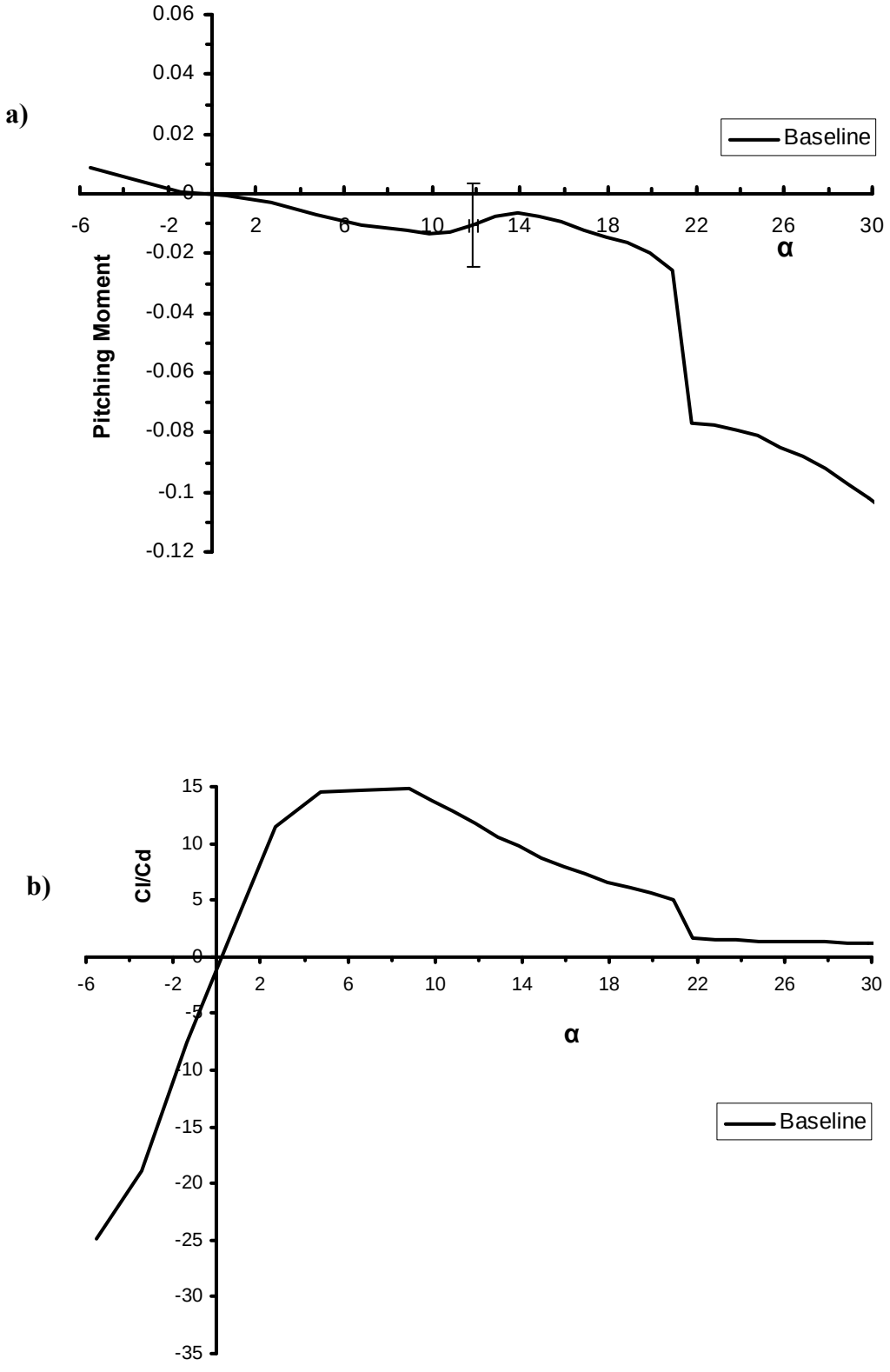

Figure 13: a) Pitching moment coefficient with error bars in place at $\alpha \approx 12°$and b) lift to drag ratio on baseline hydrofoil.

3.1.2 Effects of Protuberance Amplitude

The effect of amplitude on the performance of the hydrofoils with protuberances compared to the baseline can be seen in Figures 14-17**.** All foils with protuberances that were tested had similar lift coefficients from $-6° \leq \alpha \leq 8°$ with C_L increasing linearly as a function of α. However, beyond $\alpha \approx 8°$, all foils with protuberances showed the initial signs of separation.

The C_L of the foils with the smallest protuberance amplitude and the shortest wavelength (8S), shown in Figure 14a, follow the same trend as the baseline foil until $\alpha \approx 17°$. However, at 17°, the C_L of the foil begins to drop off with α and reaches a point where the lift is significantly lower than that of the baseline with a $C_L \approx 0.94$. As α is increased the trend stays the same, with a constant C_L until $\alpha \approx 24°$, until stall effects begin to occur and the C_L is reduced to the same value as the baseline foil. Although the lift generated by the 8S foil is generally lower than the baseline value in the pre-stall regime, the value for C_L remains fairly constant past the stall angle. Therefore, the 8S foil, with the same planform area as the baseline, it has a much less dramatic stall effect than those of the baseline foil.

As the amplitude of the protuberances is increased to medium size (8M), as shown in Figure 14a, different separation characteristics begin to appear. As in the case of small protuberances, the medium protuberances have an initial linear rise in lift with increasing angle of attack and separation begins to take place at $\alpha \approx 10°$. Separation, as in the case of small amplitude protuberances, happens at an earlier angle than the baseline foil, therefore generating less lift at lower angles. After an initial sharp drop off in lift at $\alpha \approx 14°$ the lift coefficient continues to drop off less rapidly than the baseline foil. As the

angle of attack crosses the stall angle of the baseline foil, $\alpha \approx 21°$, the 8M foil continued to generate 50% more lift than the baseline foil until at $\alpha \approx 24°$ where the lift dropped off gradually to a final value still about 16% greater than the baseline at $\alpha \approx 30°$. Overall, at most angles of attack the 8M foil had a lift coefficient which fell somewhere in between the 8S and 8L.

Large protuberances (8L), shown Figure 14a, have the greatest effect on the loads experienced by the hydrofoils. Once C_L stops rising linearly at $\alpha \approx 10°$, the lift coefficient remains nearly constant with $C_L \approx 0.82 \pm .05$ from $10° \leq \alpha \leq 26°$. This value is 28% less than the C_L max for the baseline foil, but over 40% greater than the post-stall C_L of the baseline. In essence, hydrofoils with large protuberances do not stall in the traditional sense of a rapid decrease of C_L from a maximum value.

The data for the hydrofoils with 0.50 *c,* shown in Figure 16, wavelength exhibit very similar behavior to the foils with shorter wavelengths, revealing a strong dependence of lift on the amplitude of the protuberances. The C_L for the foil with the smallest leading edge protuberances (4S) has similar values to the baseline C_L up to $\alpha \approx 15°$ before decreasing to a value of ≈ 0.8, and eventually becoming identical the post-stall C_L of the baseline foil at $\alpha \approx 26°$. The lift coefficient of the foil with the largest leading edge protuberances (4L) increases to $C_L \approx 0.80$ at an angle of $\alpha \approx 10°$ and subsequently remains fairly constant until $\alpha \approx 30°$, analogous to the 8L foil. The lift coefficient of the 4M foil once again fall somewhere in between the 4S and the 4L throughout the range of angles of attack.

The drag coefficient (C_D) of the foils with protuberances as a function of angle of attack can be seen in Figure 14b and Figure 16b. The baseline foil consistently had C_D

values either equal to or smaller than foils with protuberances. The most obvious difference between the baseline foil and foils with protuberances is that the lack of sharp increases in drag located at the stall angle. All cases with protuberances have gradual increases in drag with angle of attack and lack the dramatic increase in drag at the stall angle. As the amplitude of the protuberances is increased, the angle associated with the most significant increase in drag becomes smaller and smaller. This angle can also be associated with angles on the lift curve where slight drop-offs in lift are located indicating that some separation and stall effects might be appearing at these angles. It is noteworthy that the values for drag coefficient on foils with protuberances are significantly higher in the pre-stall regime only. However, in the post-stall regime of the baseline, the values for drag coefficient in all cases studied are very close to the values of the baseline drag coefficient, and the drag is almost independent of the leading edge geometry. This is because at high angles of attack all foils appear to be bluff.

Figure 18 shows the overall effect of leading edge protuberances on the load characteristics of the hydrofoils. Figure 18 shows the lift and drag forces on the 8L foil normalized by the lift and drag forces on the baseline foil. The 8L foil produces 28% less lift than the baseline at its lowest value in the pre-stall regime. In contrast, in the post-stall regime the lift produced by the 8L foil is as much as 50% higher over $21° \leq \alpha \leq 25°$. Drag forces on the 8L foil in the pre-stall regime can be up to 70% higher at $\alpha \approx 14.5°$, but in the post-stall regime the drag is never more than 4% greater than the baseline. This indicates that the most effective angles of attack for protuberances to be located at the leading edge of a hydrofoil are in the post-stall regime of the baseline shape. After stall

has occurred on the baseline shape, the lift can be as much as 50% higher, with little or no drag penalty.

The pitching moment coefficient (C_M) referenced to the quarter chord location for all hydrofoils are plotted in Figure 20**.** The moment coefficients for the smallest amplitude protuberance foils (4S and 8S) are generally quite close to the values of the baseline foil up to $\alpha \approx 10°$. The baseline foil has a smaller value of pitching moment than the foils with the leading edge protuberances up to the stall angle of the baseline. The pitching moments in the post-stall regime are nearly identical for all of the foils. The two foils with the largest amplitude protuberances (4L and 8L) have the largest pitching moment coefficient throughout the angle of attack range investigated. The larger pitching moments observed for the 4L and 8L foils stems from the prematurely reduced lift in the pre-stall regimes. The significant increase in pitching moment will have an impact on the design of systems employing hydrofoils employing protuberances.

a)

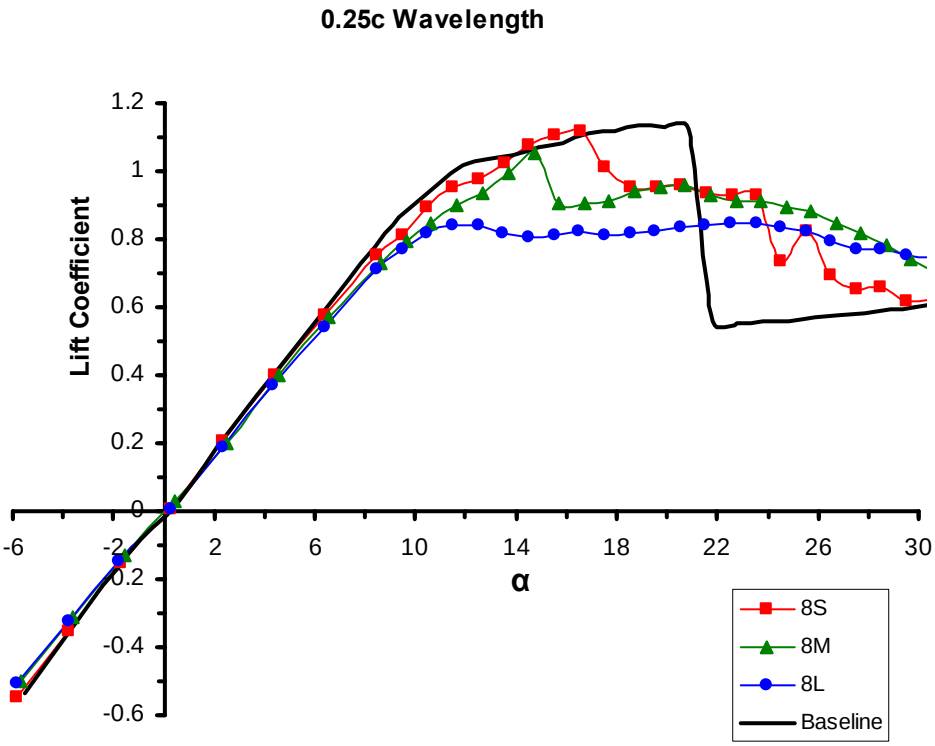

b)

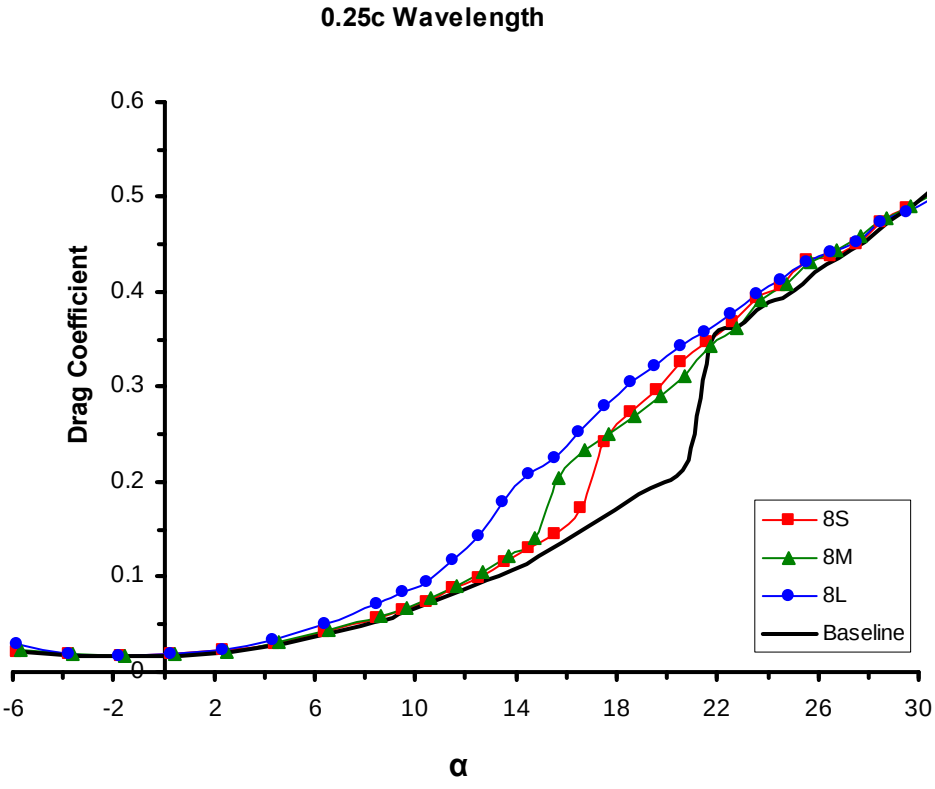

Figure 14: a) Lift coefficient and b) drag coefficient variation with angle of attack on hydrofoils with 0.25 *c* wavelength.

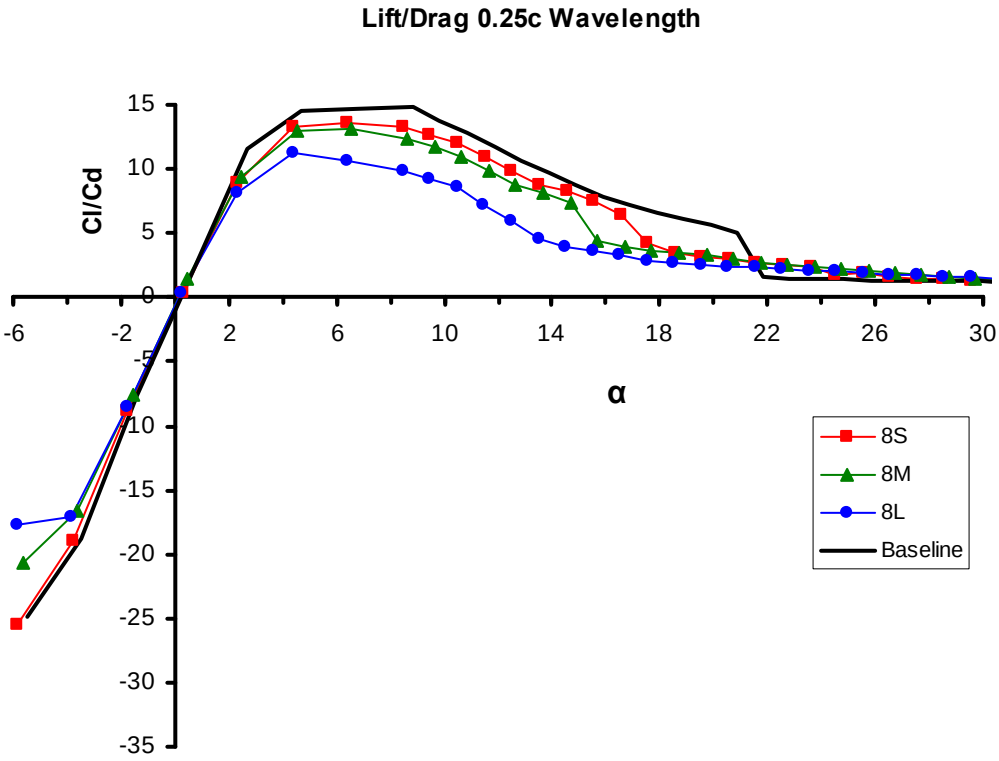

Figure 15: Lift to drag ratio variation with angle of attack on hydrofoils with 0.25 *c* wavelength.

a)

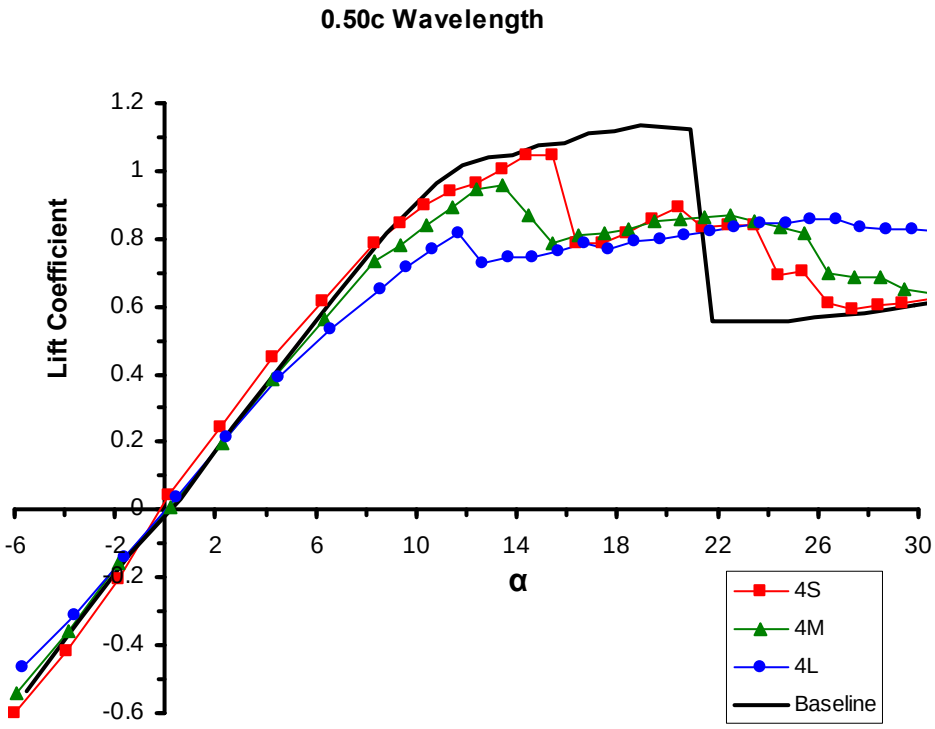

b)

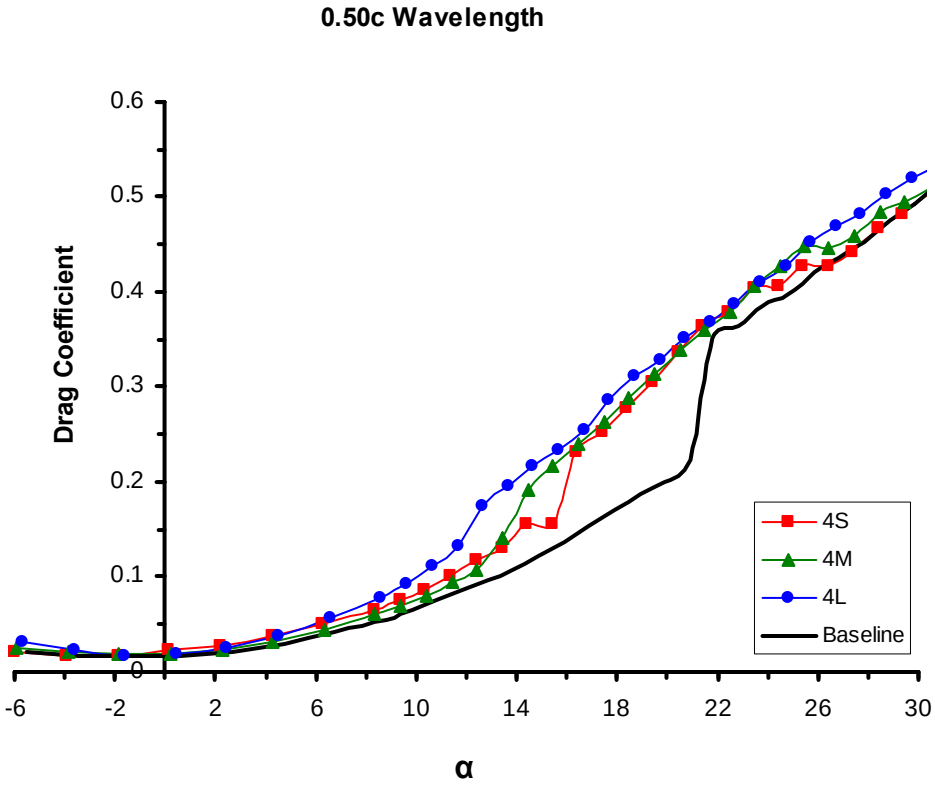

Figure 16: a) Lift coefficient and b) drag coefficient variation with angle of attack on hydrofoils with 0.50 *c* wavelength.

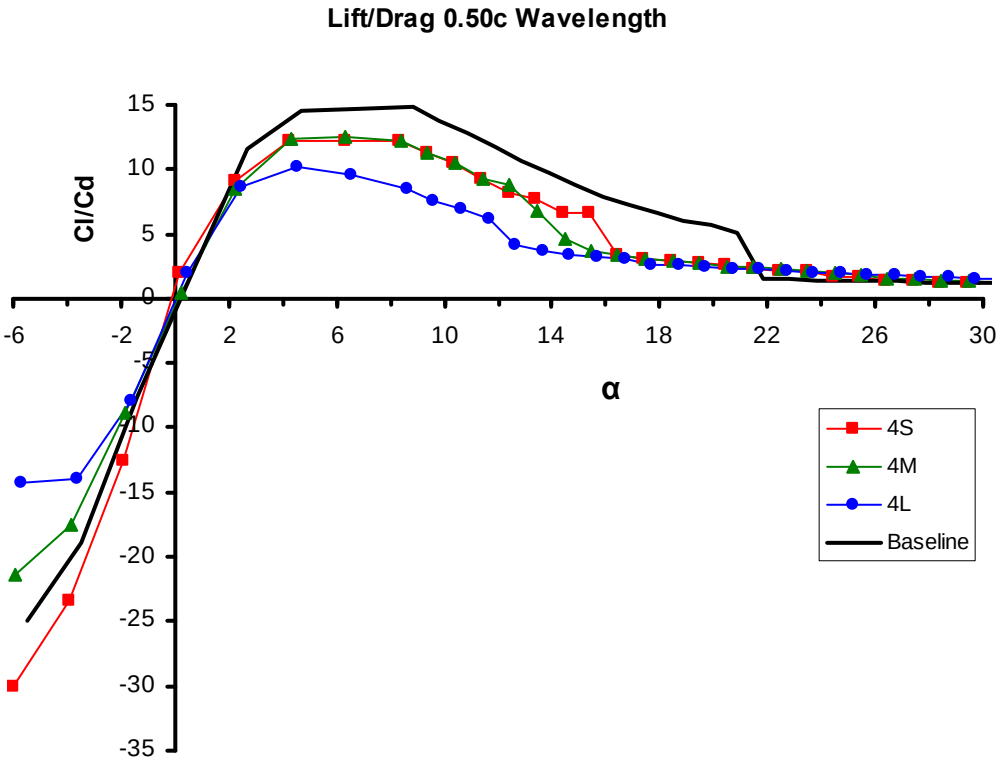

Figure 17: Lift to drag ratio variation with angle of attack on hydrofoils with 0.50 *c* wavelength.

a)

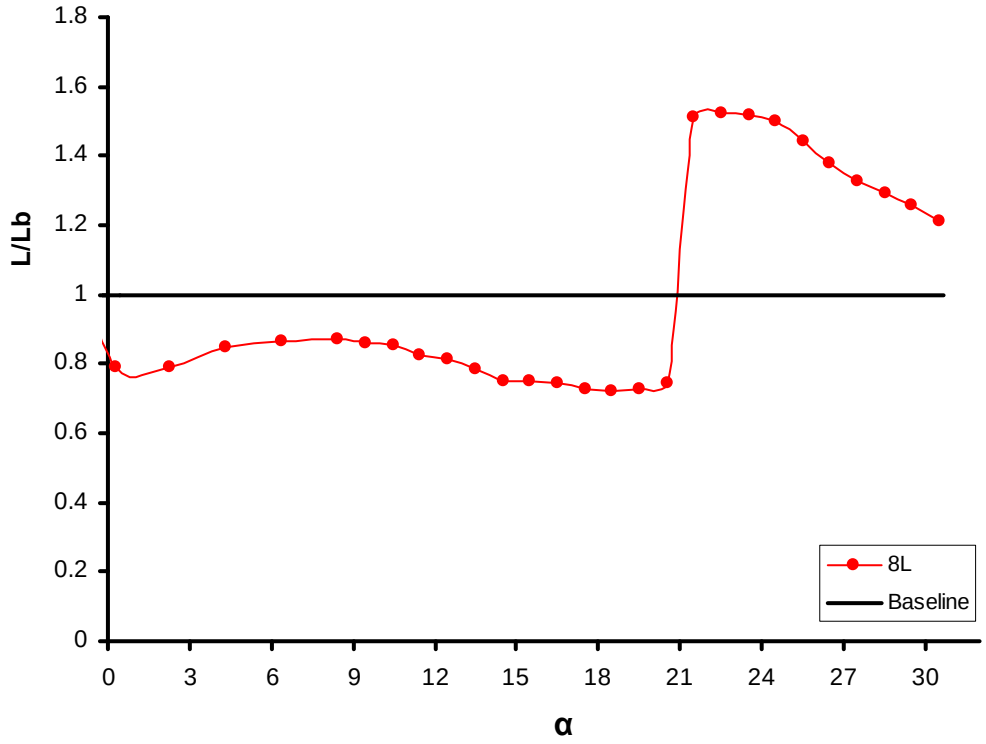

b)

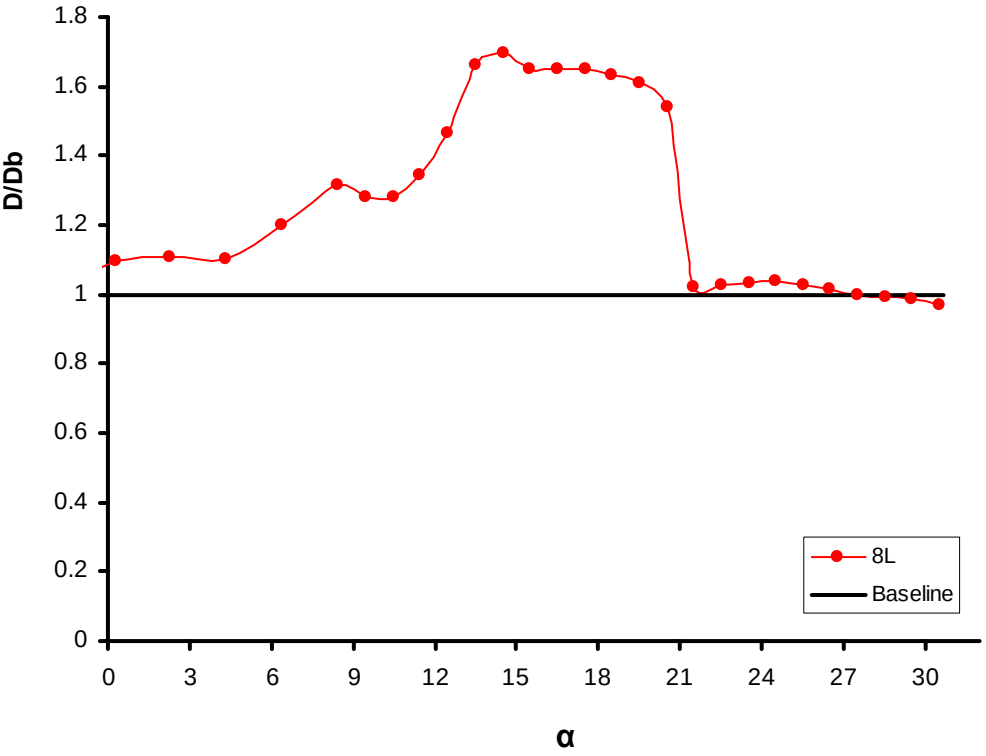

Figure 18: a) Lift and b) drag of the 8L foils normalized by baseline values.

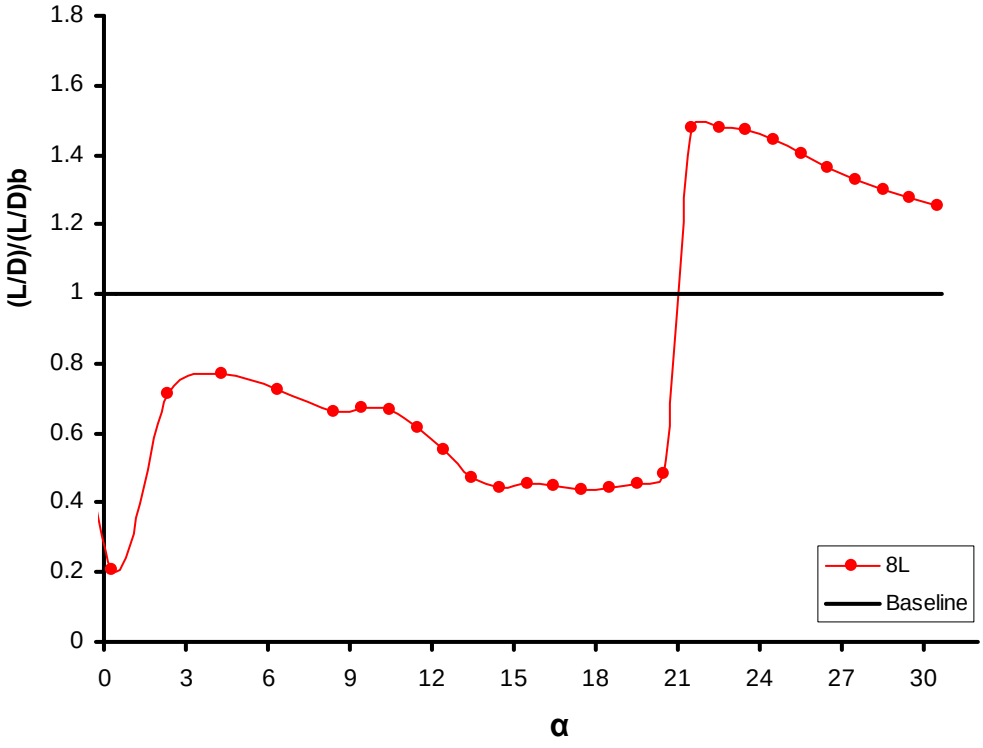

Figure 19: Lift to drag ratio of 8L foil normalized by baseline values.

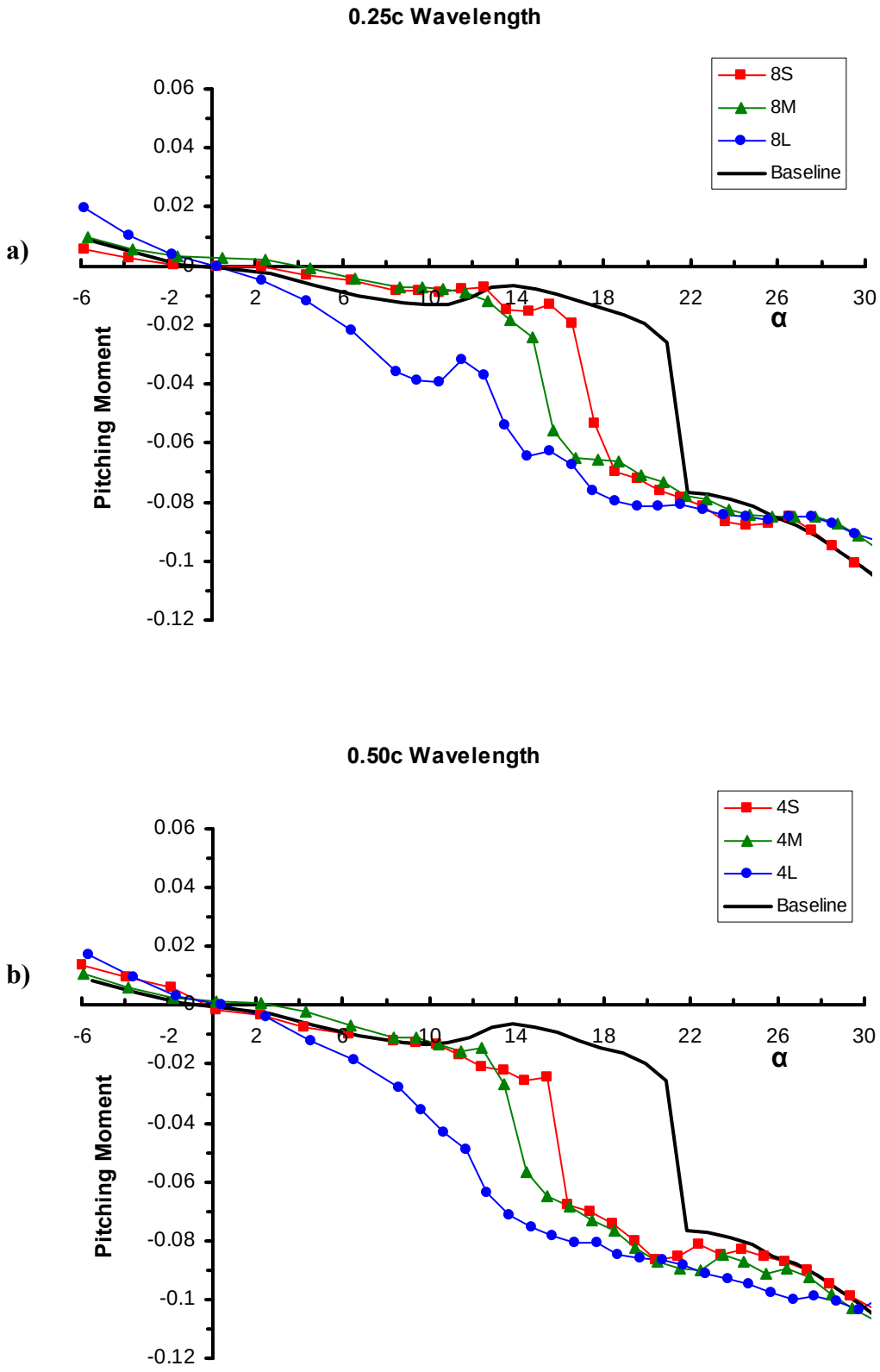

Figure 20: Pitching moment coefficient variation with angle of attack

3.1.3 Hydrodynamic Characteristics

The hydrodynamic characteristics, including the lift curve slope ($dC_L / d\alpha$), maximum C_L, α at maximum C_L, minimum C_D, maximum *L/D*, α at maximum *L/D*, and the stall angle of the hydrofoils can be seen in Table 1. The slope of lift coefficient, $dC_L / d\alpha$, within the linear range for all the foils is listed in Table 1. With the exception of 4S foil, all the foils with leading edge protuberances had lower lift coefficient slopes than the baseline foil had. Moreover, $dC_L / d\alpha$ decreases with protuberance amplitude for both wavelengths. The lowest lift curve slope of 0.081 was found for the 4L foil (0.5 c wavelength and 0.12 c amplitude). The values in Table 1 can be compared with the theoretical value of 0.11 per degree for ideal two-dimensional thin airfoils.

Table 1: Hydrodynamic characteristics of all hydrofoils tested.

airfoil	$dC_L / d\alpha$ (per deg)	*Max* C_L	α *at Max* C_L (deg)	*Min* C_D	*Max L / D*	α *at Max L / D* (deg)	*Stall* α (deg)
Baseline	0.094	1.13	20.9	0.016	14.8	8.81	20.9
8S	0.091	1.12	16.6	0.019	13.6	6.41	16.6
8M	0.086	1.05	14.7	0.018	13.1	6.58	14.7
8L	0.085	0.85	23.5	0.018	11.2	4.36	-
4S	0.099	1.05	14.4	0.022	12.3	6.30	15.4
4M	0.090	0.96	13.4	0.019	12.5	6.34	13.4
4L	0.081	0.86	26.7	0.019	10.2	4.52	-

3.1.4 Effects of Protuberance Wavelength

The effect of the wavelength of the leading edge protuberances on the load characteristics could be found from the data presented earlier. A comparison between the two wavelengths and the baseline for the three different amplitudes can be seen in Figures 21-23a. In general, the difference between the two wavelengths is small. For example, the lift coefficients for the two largest amplitude foils, the 4L and 8L, differ by no more than 10%, except at $\alpha \approx 13°$. On foils with the smallest amplitude protuberances, it is shown that the longer wavelength causes the angle of maximum C_L to drop by 2°. For foils with medium size amplitudes, the long wavelength (4M) foil has an angle of maximum C_L that is about 1° less than that of the shorter wavelength foil (8M).

The drag coefficients for the two different wavelengths are contrasted in Figures 21-23b**.** Similar to the lift coefficient trend, the effect of protuberance wavelength is minor. Nonetheless, it appears that foils with shorter wavelength protuberances generate slightly less drag than longer wavelength foils over the majority of angles of attack examined. The effect of wavelength on drag coefficient is observed to be greater for intermediate protuberance amplitude of 0.50*c* then the other two amplitudes.

a)

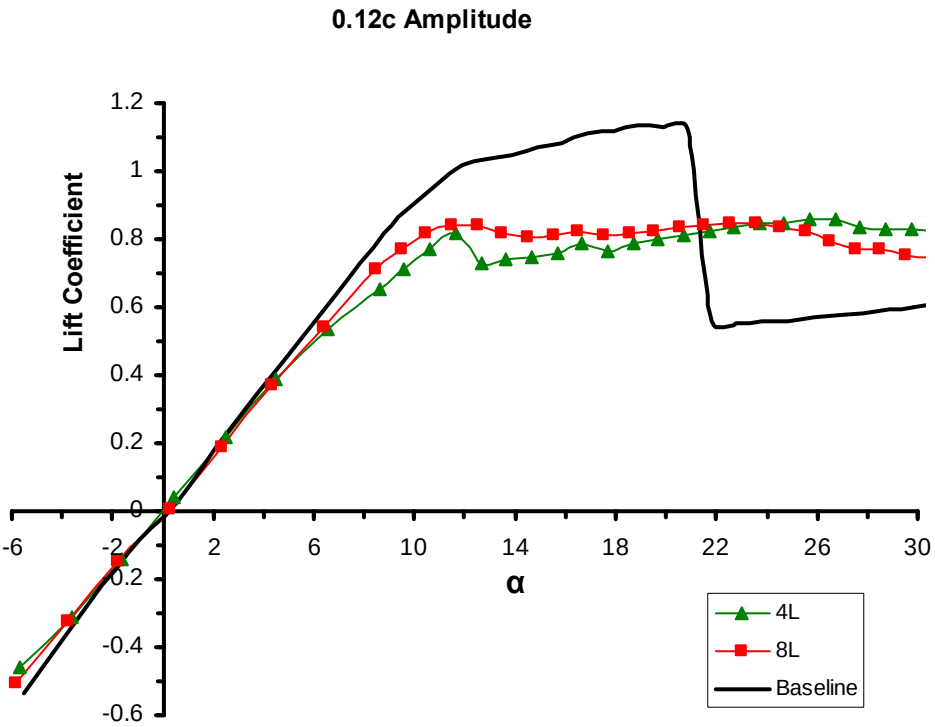

b)

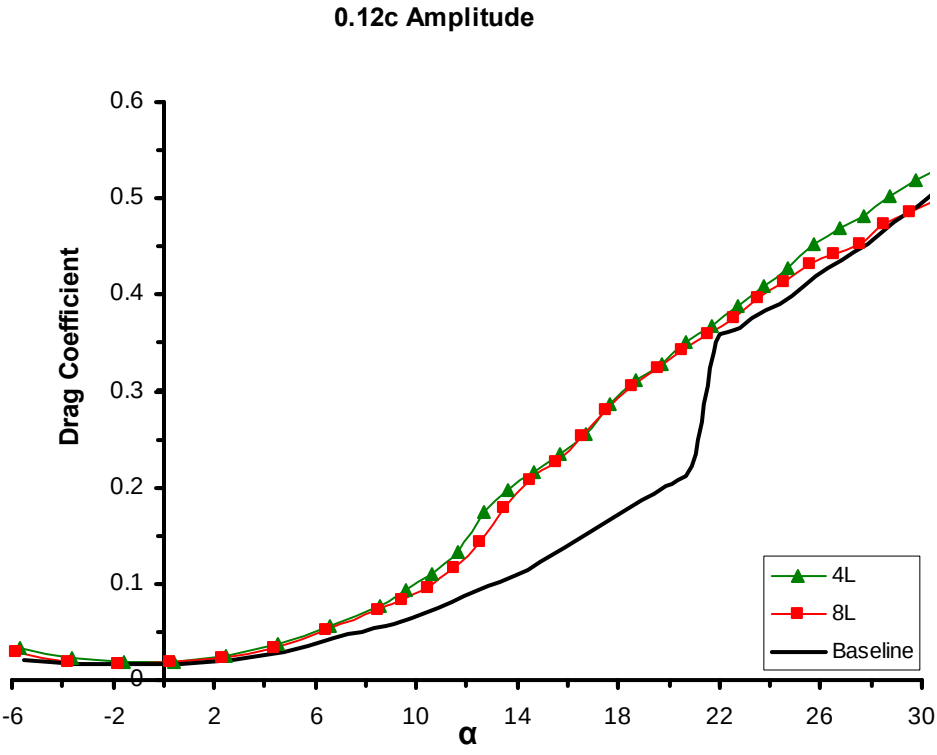

Figure 21: a) Lift coefficient and b) drag coefficient variation with angle of attack on hydrofoils with 0.12 *c* amplitude.

a)

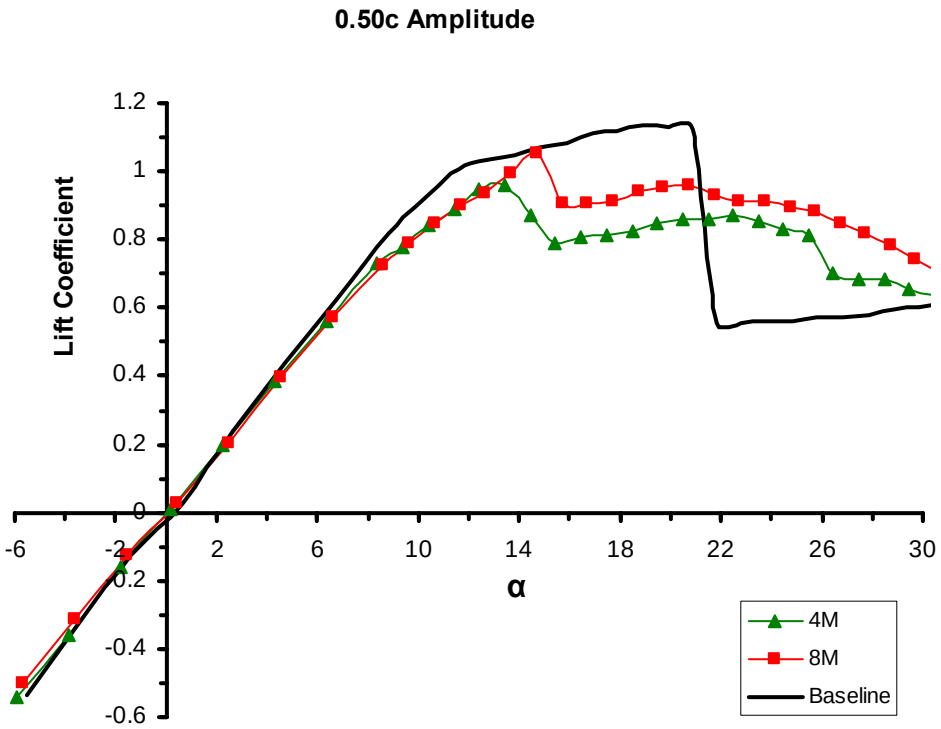

b)

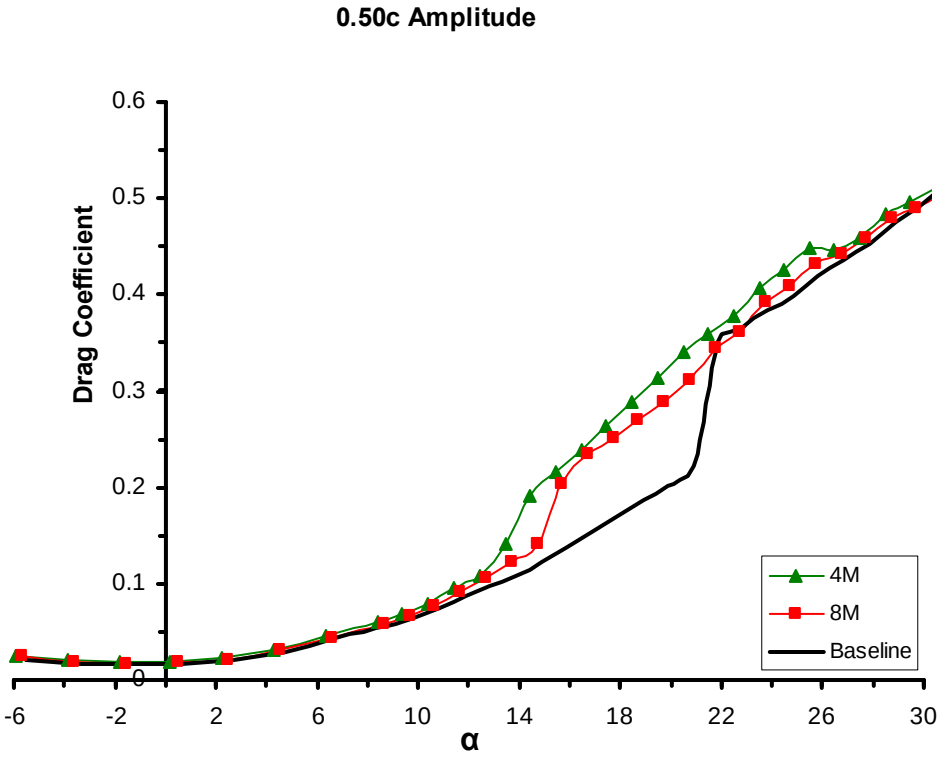

Figure 22: a) Lift coefficient and b) drag coefficient variation with angle of attack on hydrofoils with 0.05 *c* amplitude.

a)

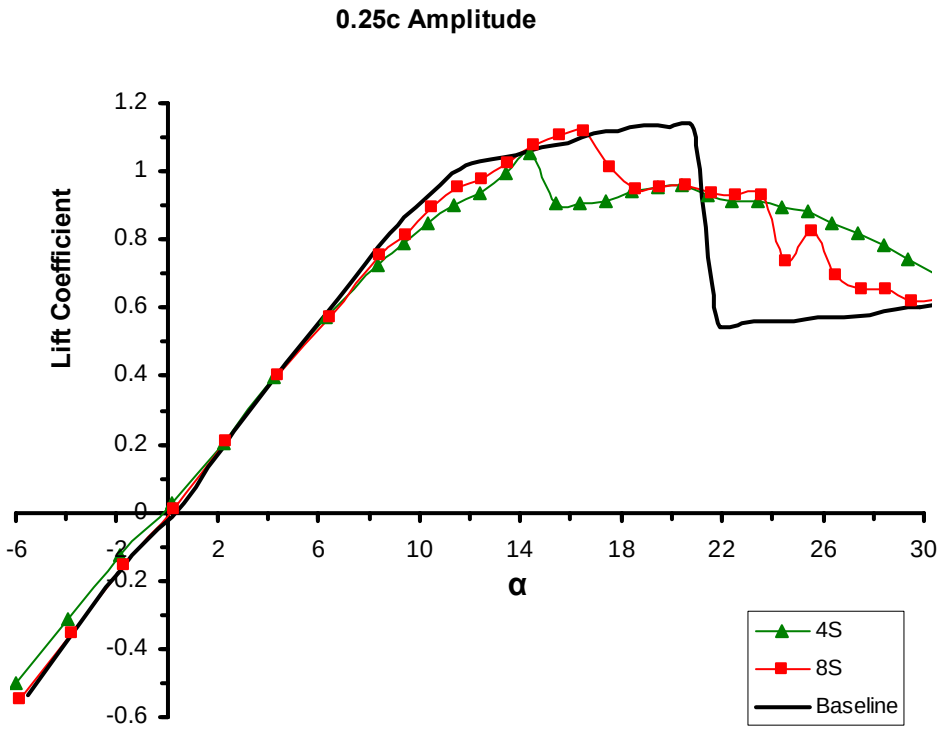

b)

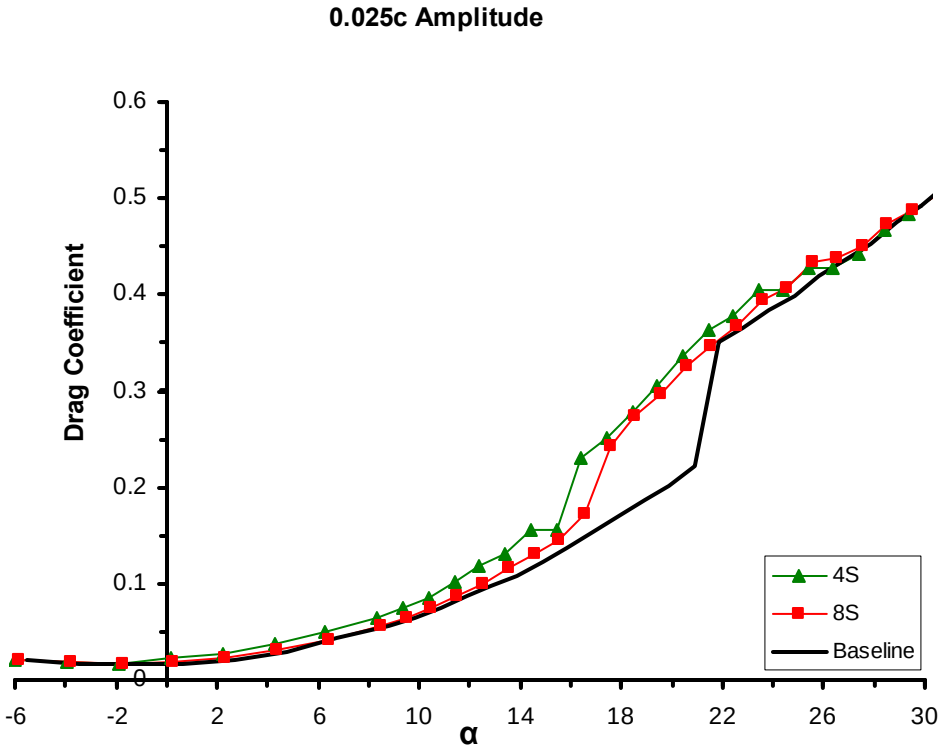

Figure 23: a) Lift coefficient and b) drag coefficient variation with angle of attack on hydrofoils with 0.025 *c* amplitude.

3.1.5 8M and 8M Hydrofoil Comparison*

A final set of load measurements were conducted to compare the 8M and 8M* hydrofoils. The lift and drag coefficients of the 8M and 8M* as a function of angle of attack are compared in Figure 24. The purpose of this experiment was to find out the difference, if any, in lift and drag between a foil with a sinusoidal leading edge geometry having the same planform area as the baseline and a foil in which the protuberances are essentially added on to the leading edge of the baseline hydrofoil. In a practical application, it is an easier task to add protuberances to the baseline shape rather than to add peaks and subtract valleys to create the protuberances along the leading edge. Therefore, it was necessary to investigate this scenario.

The data in Figure 24 shows that the differences between the two different scenarios are very small. The general trends in the lift coefficient remain the same between the 8M* foil as with the 8M. The lift coefficient of the 8M* foil never produces more than about a 6% difference in lift and never more than about an 11% difference in drag. Therefore, it can be concluded that it may be more advantageous to implement protuberances into some kind of active mechanism that adds the protuberances to the leading edge of a baseline foil shape when necessary to take advantage of the post-stall benefits of leading edge protuberances.

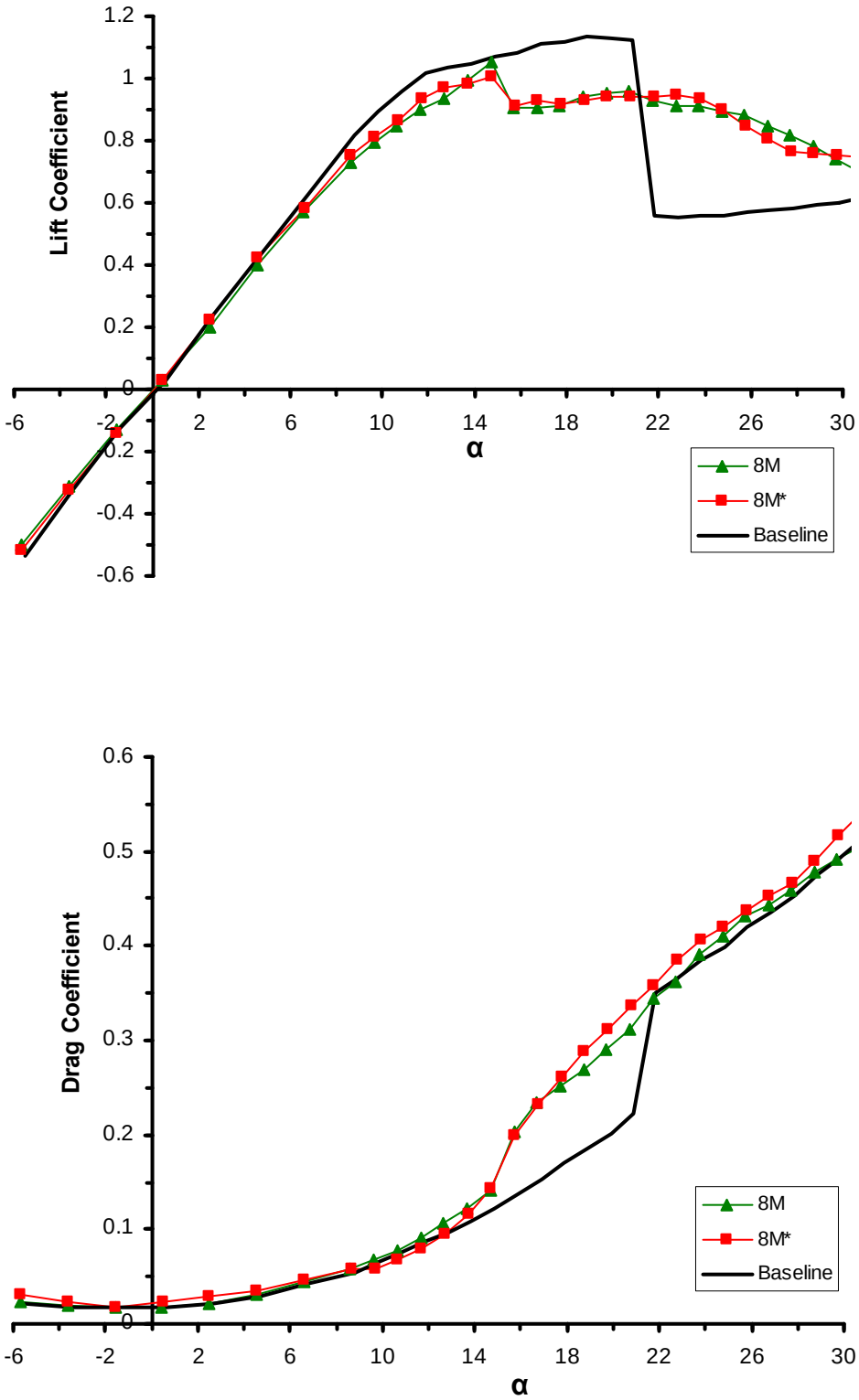

Figure 24: a) Lift and b) drag coefficient comparison between 8M and 8M* hydrofoils.

3.2 Tuft Flow Visualization

To asses the flow field near the surface of the hydrofoils, a flow visualization technique using tufts was employed on the set of large span hydrofoils (s = 305 mm). This set of hydrofoils consisted of baseline, 4M, 8M and 4L leading edge geometries. Instantaneous images of the foils at α = 0°, 12°,18°, and 24° can be seen in Figures 25 to 28 In these images only the central two-thirds portion of the foils are shown. This portion of the longer hydrofoils corresponds to the section on which the load measurements were taken. By examining the images it was possible to determine the near surface flow patterns responsible for the changes in the forces on the hydrofoils. These specific angles were chosen because at α = 12° the loads on foils with the largest protuberances begin to deviate from the baseline trend. The angles α = 18° and 24° refer to the conditions just before and after the stall of the baseline foil. The freestream speed in these experiments was 1.8 m/s, which is the same as the freestream speed used in the load measurements.

In Figure 25 the freestream flow is moving from left to right and the angle of attack is 0°. It is obvious that flow is attached to the surface of every hydrofoil at α = 0°. Almost all tufts are pointing in the downstream direction, and there is no random movement in the tufts caused by turbulence and separation over the foil. Minute amounts of spanwise flow can be seen on or near the inflection points (shoulders) of the protuberances normally in the general direction of the peaks.

Figure 26 shows the flow field at α = 12°. The initial signs of separation can be seen in all images at this angle. Separation is indicated by the chaotic, undulating, movement in the tufts. On the NACA 63_4-021 profile, separation begins from the trailing edge and creeps forward with increasing angle of attack. In the baseline case, nearly

three-quarters of the surface of the hydrofoil is attached while the remaining area is separated to the trailing edge. The same general trend holds in the cases with protuberances; there is separation occurring at the trailing edge, although in the cases with protuberances there is up to 25% more separation, covering the entire surface of the foils. Beginning from the leading edge of the 4L foil, separation can be seen in the form of a cell that begins at the leading edge of the center valley and propagates to the trailing edge. By comparison there is much more separation in the 4L case than the baseline case. This correlates very well with load measurements which indicated that there was reduced lift in comparison to the baseline foil at this angle. The 4M foil shows a similar pattern to the 4L in that there are cells of separation once more. Cells can once again be detected behind the leading edge of the three valleys in the image. Although it is not in the form of a single cell, separation still appears behind the valleys in the leading edge. The 4M hydrofoil retains more attached than the 4L foil, correlating well once more with load measurements. The 8M foil follows the same general trend as the 4M foil at 12°. There are cells of separation near the trailing edge of the foil, but these cells are not behind every valley. As shown in Figure 21 there is not much difference in the load measurements between the 0.25 *c* and 0.50 *c* wavelengths. This is shown by the very similar separation characteristics between the 4M and 8M foils.

At 18° shown in Figure 27 separation can be seen up to the 0.5 *c* point of the baseline foil. By comparison, all foils with protuberances have more separation than the baseline. Whereas the baseline foil has a “line” of separation, at higher angles, large cells of separation can be seen on foils with leading edge protuberances. The 4L foil has fully separated flow in all of the valleys shown in the image. General trends in spanwise flow

also begin to appear at these higher angles. Subtle signs of fluid flow towards and away from valleys can be seen in the images. Flow appears stalled in the center of the 4L foil directly behind the valley, but further examination reveals that there is movement of fluid from the neighboring peaks towards the valleys. Spanwise flow is most clearly seen in the row of tufts extending from the neighboring peaks. On either side of the valley fluid movement from the neighboring protuberances toward the valley can be seen extending to the neighboring peaks. Neighboring valleys reveal the opposite trend; flow moving away from the valleys and towards neighboring peaks. Separation cells stemming from the valleys appear to be bi-periodic in that, if one valley has a specific trend of spanwise flow pattens, it isn't the neighboring valley that shows the same pattern, but the second valley away from it. Although the peaks have definite spanwise flow, the second valley away, rather than the neighboring valley, shows the same trend. On all peaks of the 4L foil flow remains attached at 18°. Whereas the 4L foil has much more separated flow than the baseline at this angle, attachment was always retained on the peaks of the protuberances. In all cases with protuberances the cells of separation stem from the valleys and spread out linearly as the trailing edge is approached. At 18°, the 4M foil also shows signs of separation in the form of cells. For the most part the 4M foil is separated but, similar to the 4L foil, protuberance peaks still preserve flow attachment. Over the span, separation appears behind valleys but the trend is bi-periodic once again, the center valley attracting fluid, and the neighboring valleys repelling it. The 8M foil displays the same pattern shown with other leading edge protuberance foils at this angle. The 8M foil has a larger attachment region which causes the lift on this foil to be higher than those of

the other foils; this once again correlates well with load measurements. The 8M foil has similar flow characteristics as the 4M foil as well as load characteristics.

The post-stall angle of $\alpha = 24°$, shown in Figure 28**,** reveals the most significant deviation in flow pattern between foils with leading edge protuberances and the baseline. At 24° the flow over the baseline foil has completely separated, and the baseline is considered stalled. The flow patterns over all of the other foils remain nearly the same as they were when the angle of attack was 18°. In all cases, nearly all secondary flow remains the same; all general trends that were seen in the valleys are still occurring at 24°. The most important aspect seen in the flow pattern is that the peaks on all foils still retain attached flow. It follows from the load measurements that this should be so because between 18° and 24° the lift measurements remained nearly unchanged. Also, attachment at this angle ensures that the lift coefficient for foils with leading edge protuberances is higher than the baseline.

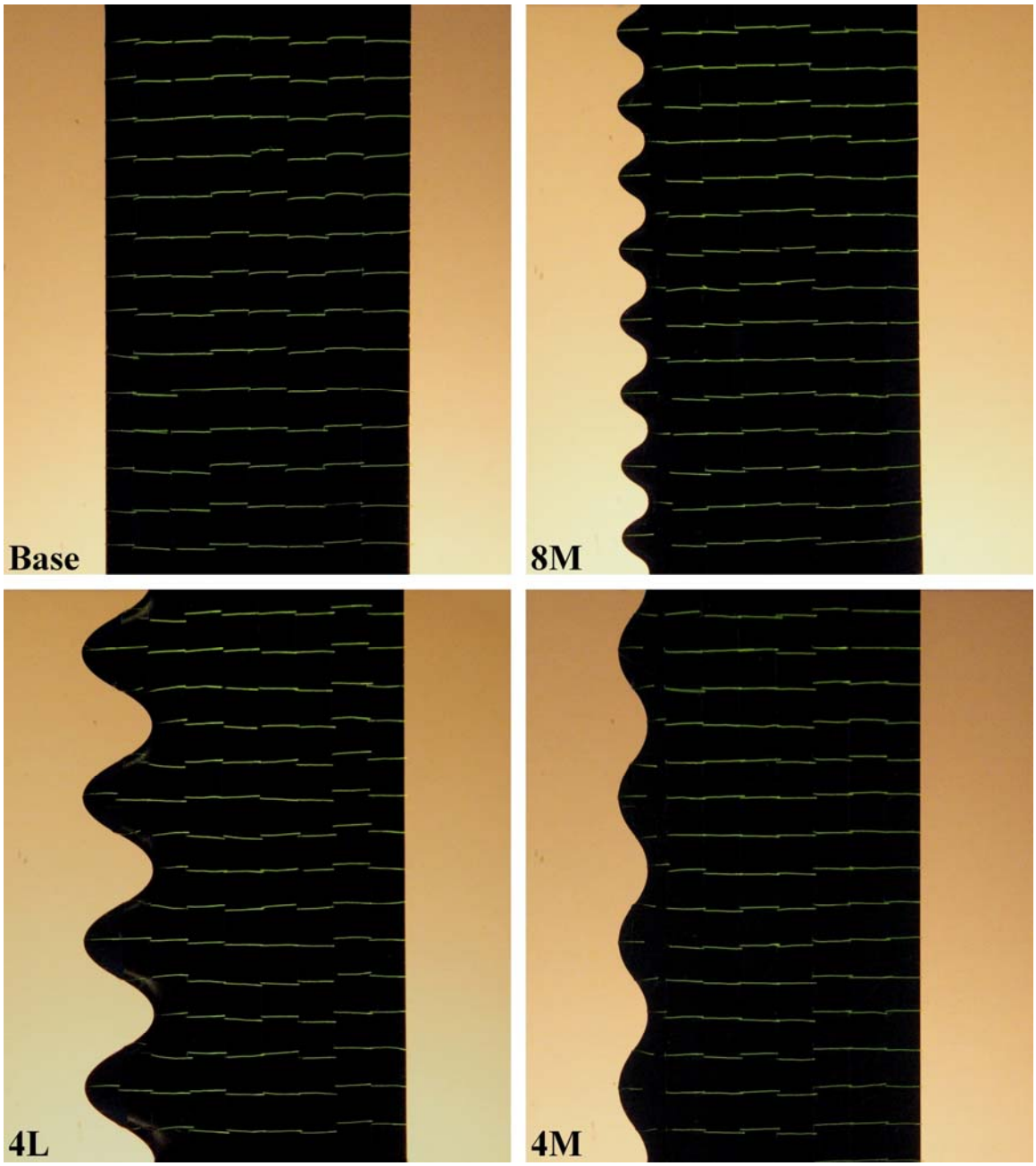

Figure 25: Tuft flow visualization, α = 0°.

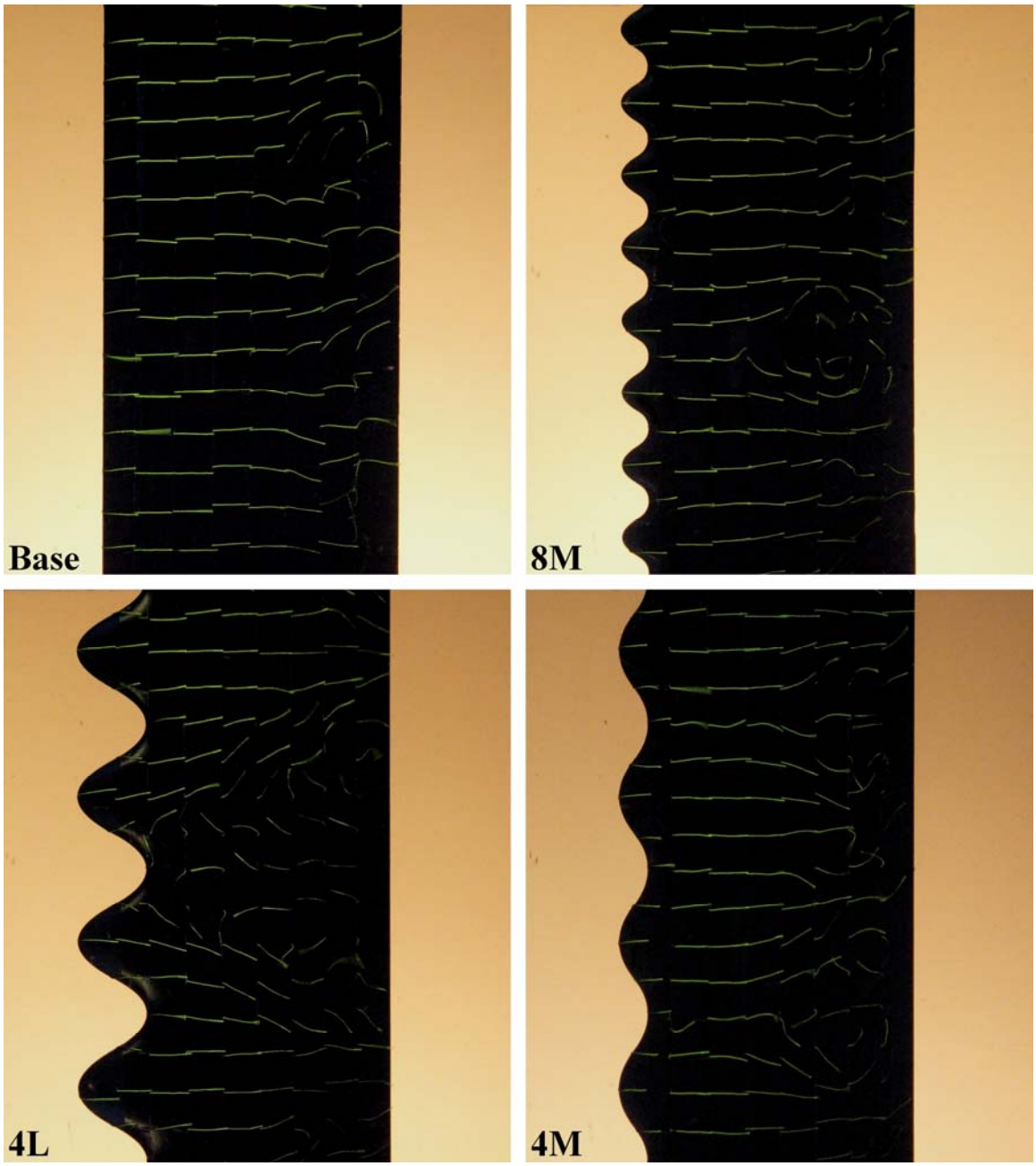

Figure 26: Tuft flow visualization, α = 12°.

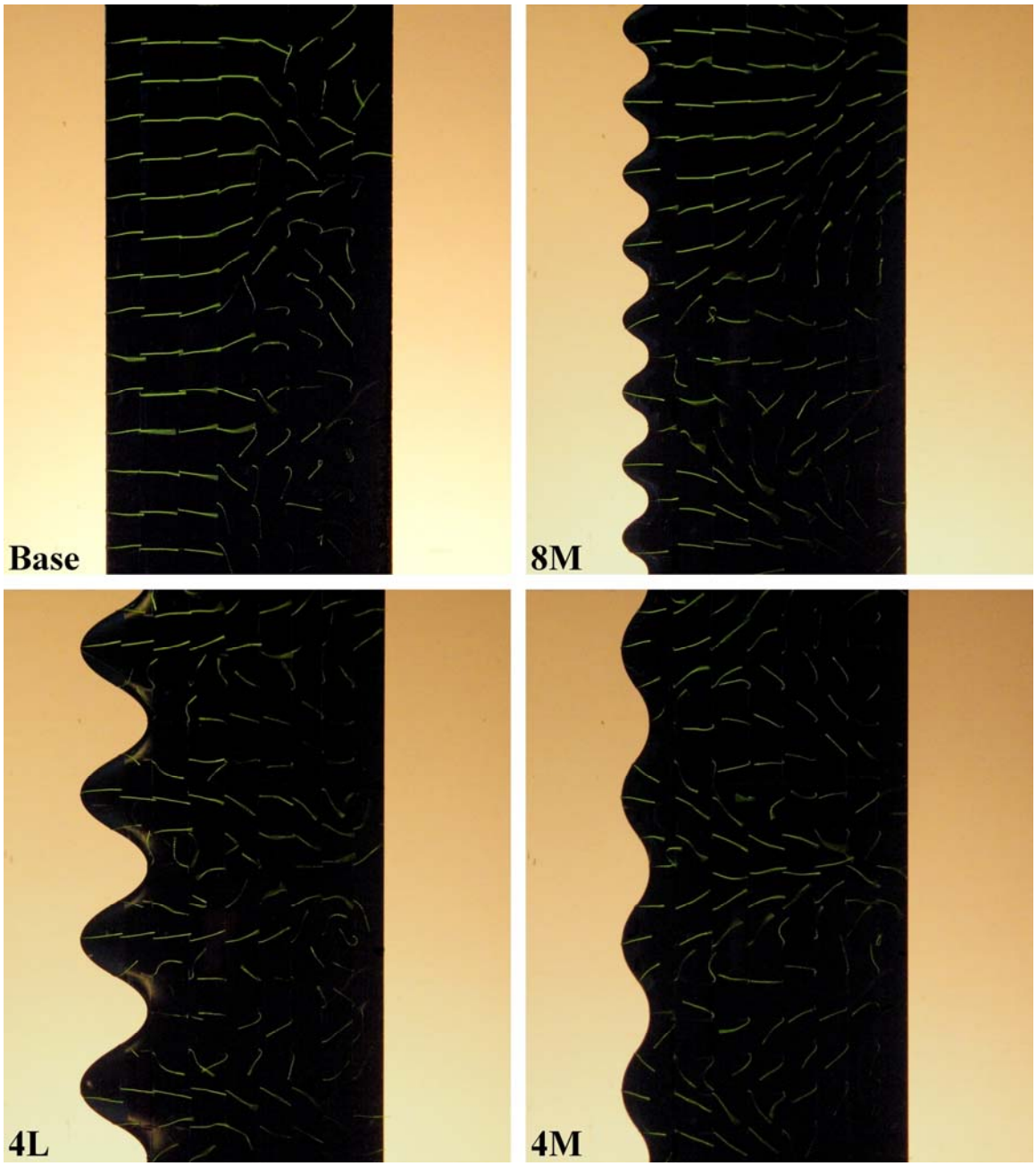

Figure 27: Tuft flow visualization, α = 18°.

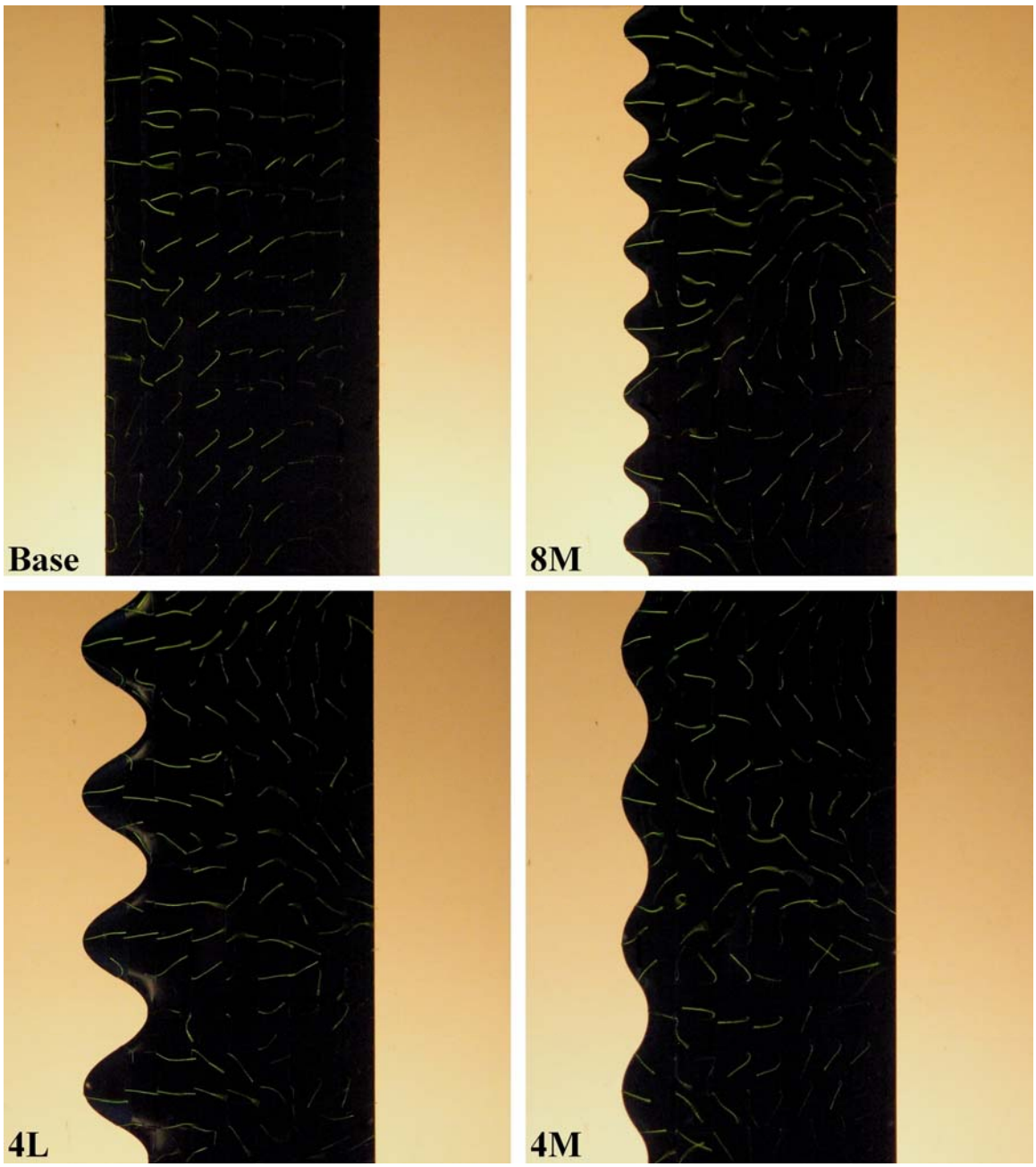

Figure 28: Tuft flow visualization, α = 24°.

3.3 Dye Flow Visualization

Dye was used as another form of flow visualization to examine the near surface flow field over the low pressure side of two foils, the baseline and 4L. The use of dye allows for a detailed view of the flow structures that that surround the hydrofoils. Similar to the tuft experiment, four angles of attack were once again used, α = 0°, 12°, 18°, and 24°.

Figure 30 shows a comparison of the baseline foil and the 4L foil at α = 0°. The dye streams exit the leading edge of the foils in laminar fashion and move downstream with the freestream flow. In the baseline case, the streams move in straight lines toward the trailing edge until a certain point along the chord is reached and the dye begins to break up. This break-up caused turbulence near the trailing edge. Also, it is worth mentioning there is an insignificant amount of spanwise flow, which indicates that the fences bounding the ends of the hydrofoil create a 2-D flow field. The flow patterns seen in the baseline image are as to be expected at 0°.

Similar to the baseline flow patterns, the flow patterns in the 4L image show that the dye once again diffuses as it reaches the trailing edge of the hydrofoil; however, in contrast to the baseline flow patterns, those in the 4L image show significant spanwise flow even at 0°. Symmetry is seen between the valleys and the peaks of the foil, and the dye streams coming off of the inflection points of the protuberances show signs of vortical structures with streamwise vorticity. Using the images as reference vortices spin counter-clockwise (ccw) on the bottom shoulders of protuberances and clockwise (cw) on the upper shoulders of the protuberances. In essence, on each protuberance is an indication that there are counter-rotating vortices coming off of the inflection points.

Another noteworthy feature of the 4L flow pattern is that there are coalescences of dye behind every valley and divergences of dye streams behind the peaks. This indicates that relative to the area behind the peaks a lower pressure system exists behind the valleys at any chordwise position. Fluids have a tendency to move from high pressure to low pressure. This is discernible in Figure 30 by a general pattern of fluid at about the ¾ chord point toward moving toward the valleys.

At α = 12°, shown in Figure 31, the line of separation on the baseline foil has moved closer to the leading edge, and now resides at about the 0.5 *c* point. However, the 4L image shows a separation line at about the 0.33 *c* location, which is discernible by the difference between the laminar and turbulent dye flow patterns. Furthermore, the 4L flow patterns show major signs of spanwise flow. In contrast to 0°, the flow field is no longer periodic from peak to peak and valley to valley, but is now bi-periodic. The upper half of the foil is reflected about the center axis. It can now be seen that there is a divergence, rather than a coalescence, of dye in the center valley, whereas the valleys above and below the center of the foil contain coalescences of dye behind the valleys. Although the general appearance of the flow field is different, the sign of the vortices that stem from the inflection points is the same as at 0°, with lower inflection points having counter-clockwise vorticity, and upper inflection points having clockwise vorticity. The fact that dye disperses in the center valley as soon as it leaves the leading edge of the hydrofoil indicate that there is flow interaction between neighboring valleys. Essentially, the vortices in one valley become strong enough to change the patterns of the neighboring valley through interactions between the vortices. This interaction occurs in all of the valleys and equilibrium is eventually reached.

At 18°, shown in Figure 32, patterns similar to those seen at 12° emerge. The baseline is at an angle just prior to stall and this can be seen by the fact there are significant amounts of separation and attachment is only retained near the leading edge. Separation has also increased on the 4L foil. The most significant difference between 12° and 18° is that every valley has now stalled even though there are still patterns of coalescence and divergence in the valleys. The general flow patterns seen at 12°, which consisted of a dye stream divergence in the center of the foil and coalescence in each of the neighboring valleys, has remained the same, but the point of coalescence has moved closer to the leading edge, and the divergence pattern has widened. Also, the magnitude of the vortices stemming from the inflection points of the protuberances has increased. Attachment is still retained on all of the peaks.

At 24°, shown in Figure 33, the baseline foil has completely stalled. This is shown by the dye streams diffusing immediately after they leave the leading edge and turn into an array of vortices with spanwise vorticity that are shed at the leading edge. Similar to the flow patterns over the 4L foil at 18°, the points of coalescence have once again moved toward the leading edge, and the angle of divergence of dye in the center valley has once again widened. The magnitude of the vortices stemming from the protuberance inflection points has increased once more as well. This was determined qualitatively by visual indications of an increase in angular velocity of the vortices. The most significant difference between the 4L and baseline foils at $\alpha \approx 24°$ is the fact that even though the baseline has lost flow attachment all the way to the leading edge, the 4L has retained attachment on all of the peaks and inflection points.

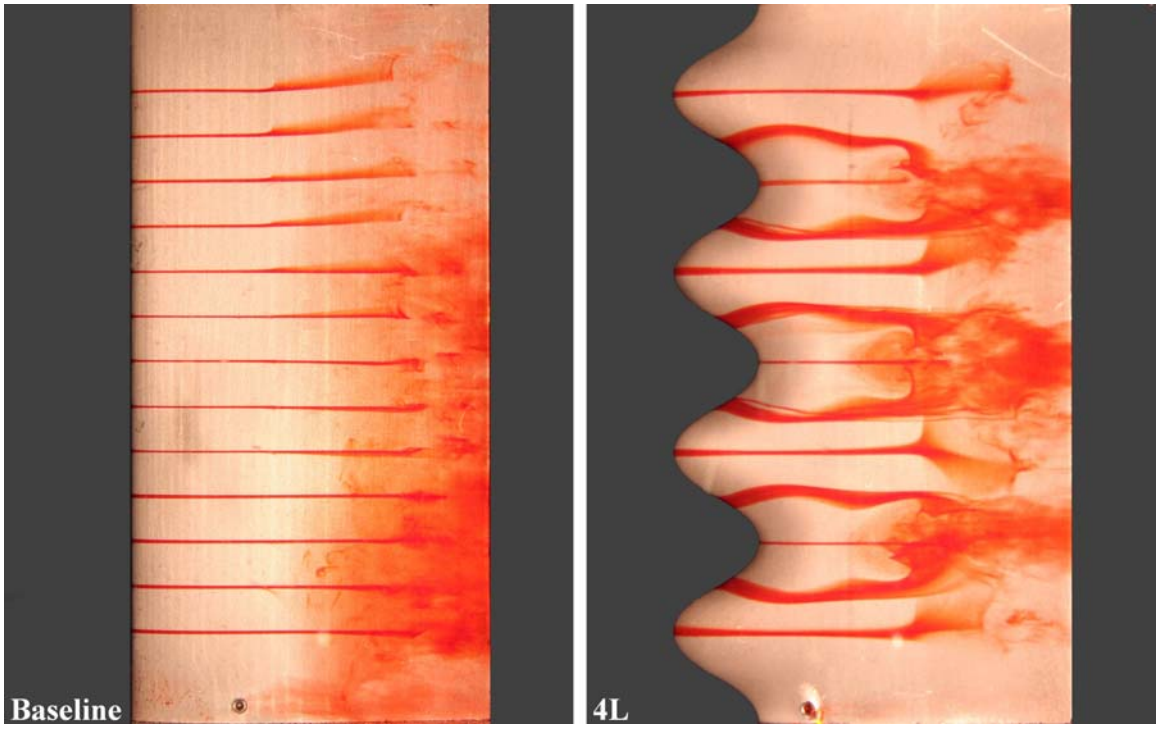

Figure 30: Dye flow visualization, α = 0°.

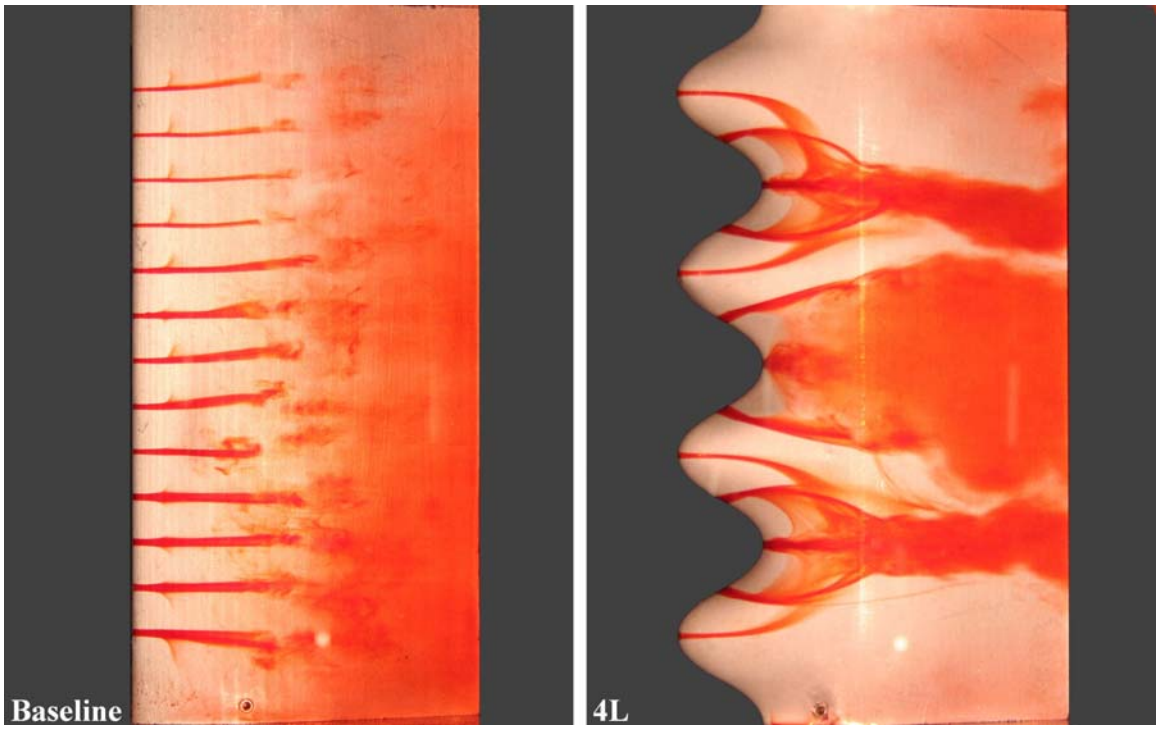

Figure 29: Dye flow visualization, α = 12°.

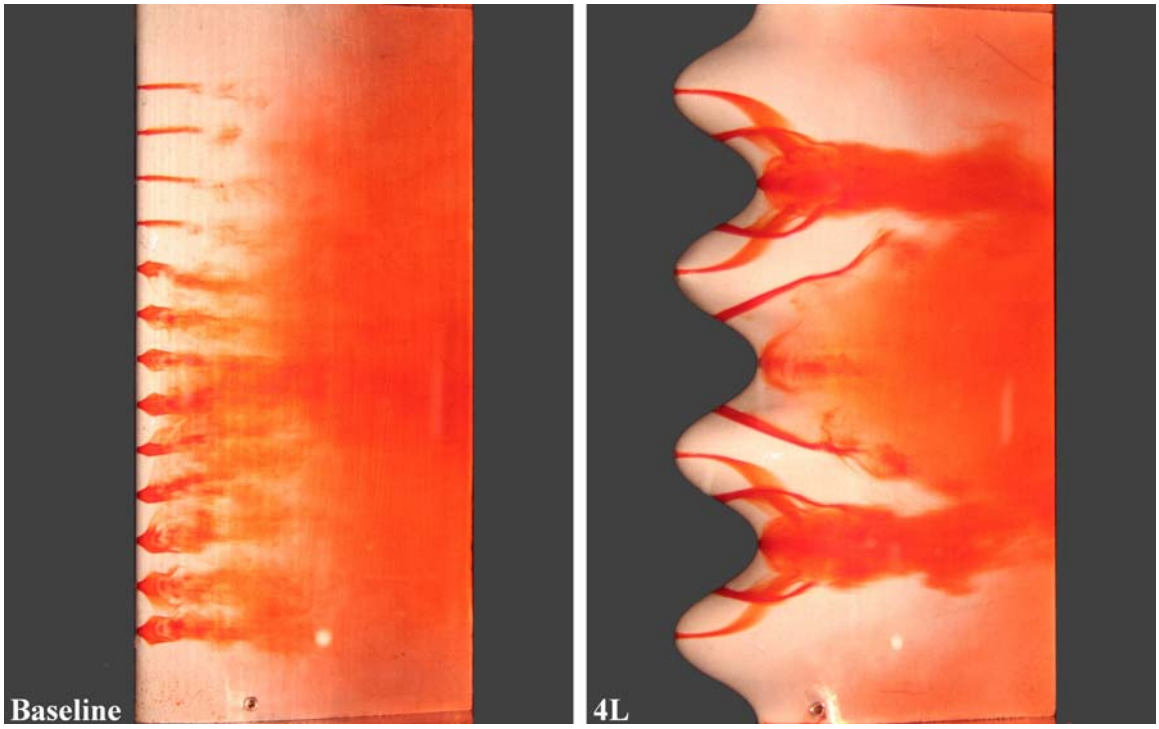

Figure 31: Dye flow visualization, α = 18°.

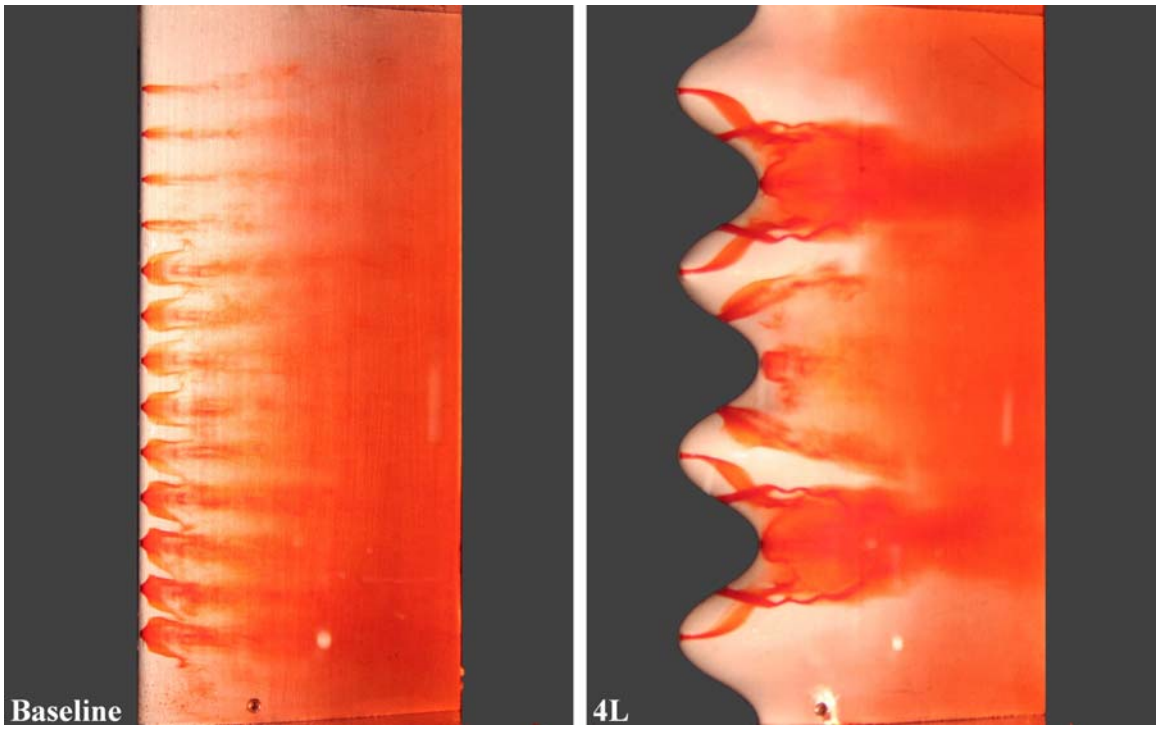

Figure 33: Dye flow visualization, α = 24°.

4 Discussion

The hydrodynamic load characteristics of a hydrofoil with protuberances are quite different than those of a straight, smooth leading edge hydrofoil of equal planform area. It was shown that in the pre-stall regime (of the baseline foil) hydrofoils with protuberances generate lower lift and higher drag. In the pre-stall regime it is obvious that it is more advantageous to retain baseline leading edge geometry. However, in the post-stall regime the load characteristics of foils with leading edge protuberances are significantly more beneficial than without protuberances. This indicates that an active mechanism which deploys protuberances in post-stall regime of the baseline is a necessity to take full advantage of the protuberances. By doing this, a control surface can benefit from both the increased lift and lower drag created by the baseline shape in the pre-stall regime, while in the post-stall regime retain lift without the sacrifice of added drag.

Flow visualization experiments show significant differences in the flow field surrounding foils with protuberances as opposed to the baseline leading edge. The presence of protuberances along the leading edge effectively creates a varying leading edge sweep angle along the span. This in turn introduces spanwise flow along the leading edge in the form of streamwise vortices. These vortices result in low pressures along the foil surface and are responsible for generating added lift past the stall angle of the baseline foil. This effect is also seen on a delta wing, in which case vortices are generated along the edge of the wing creating a low pressure system on the surface of the wing. A delta wing uses the counter-rotating vortices to generate lift at high angles of attack at low speeds. However, for the foils studied here and at pre-stall angles of attack, the lift generated by the vortices stemming from the protuberances is not sufficient to overcome

the loss of attached flow still present on the baseline foil. Larger regions of separation on foils with protuberances are the main cause of lower lift coefficients at pre-stall angles of attack. In all of the flow visualization experiments, it is evident that in the pre-stall regime there is less flow attachment, resulting in reduced pressure differences across the hydrofoil surface than the baseline foil for equivalent angles of attack.

The vortices stemming from the protuberances also cause low pressure in the valleys of protuberances. Normally, on a flat surface counter-rotating vortices will tend to move away from each other because of their images, but due to the geometry of the hydrofoils with protuberances, the vortices stemming from the protuberances rotate in a way that causes them to migrate towards the valleys causing a coalescence of fluid between protuberance peaks. This can clearly be seen in Figure 34 in the upper and lower valleys. Because of low pressure in core of these vortices, they combine to create low pressures in the valleys of the protuberances. At high angles of attack separation at the trailing edge of the foils tends to interact with flow at the leading edge causing unstable asymmetric flow patterns, seen in the center valley in Figure 33. This creates differing patterns from valley to valley. The patterns are unstable and are related to the fluctuating flow field at the trailing edge of the foil. A schematic of this can be seen in Figure 34.

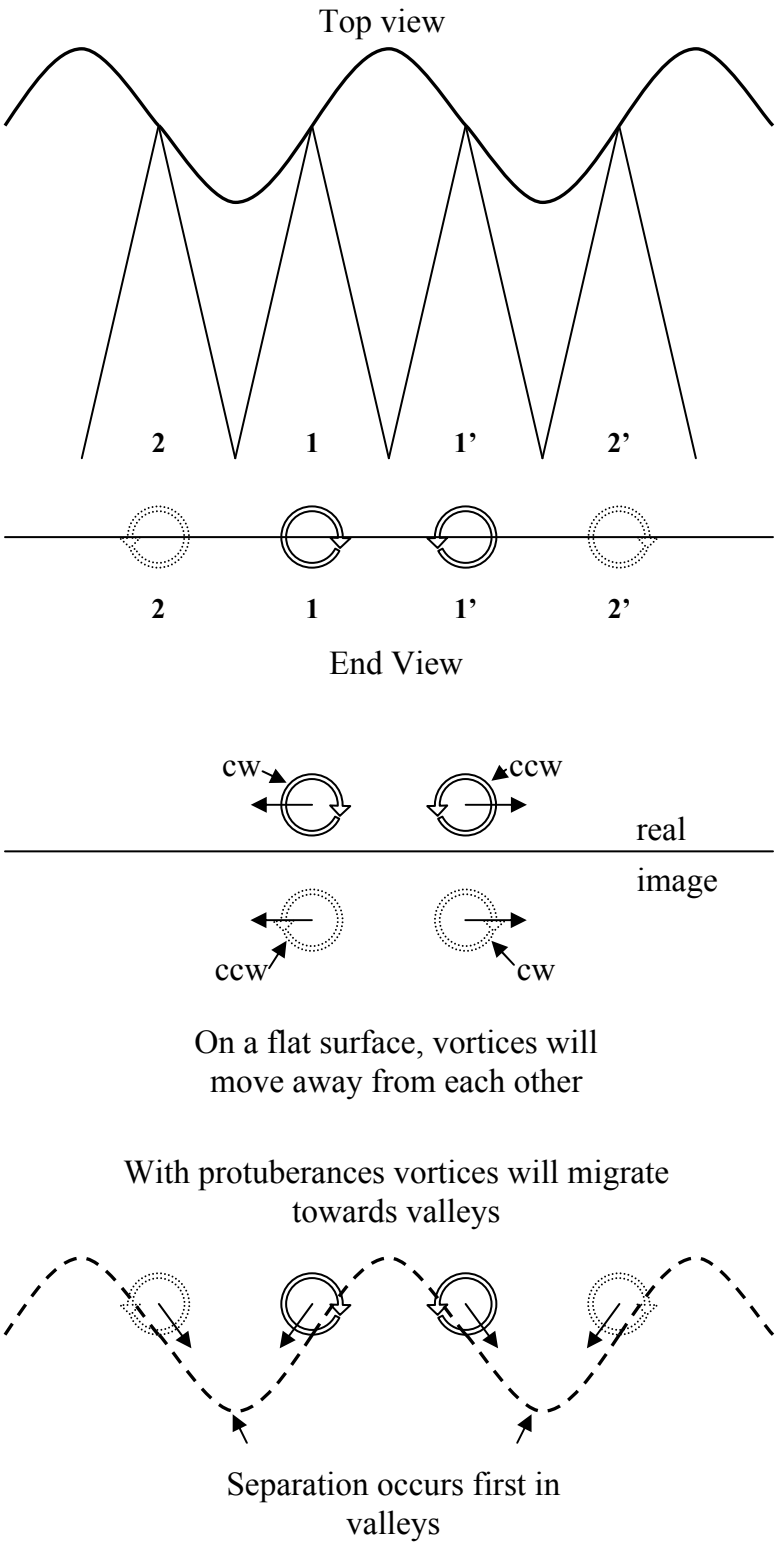

Figure 34: Schematic of the interaction of the vortices stemming from protuberances.

Although there are significant areas of separation at low angles of attack, foils with protuberances always retain flow attachment on the peaks of protuberances. The relatively higher measured lift in the post-stall regime is due to flow attachment retained on the peaks at higher angles of attack as well as the formation of counter-rotating vortices coming off of the shoulders of the protuberances. It can be clearly seen that at angles of attack in the post-stall regime, foils with protuberances retain larger amounts of attached flow (seen in sections 3.2 and 3.3) as well as higher lift coefficients (seen in section 3.1.2).

The amplitude of the protuberances plays a major role in establishing the characteristics of the hydrofoils with leading edge protuberances. This is likely caused by differences in the strength of spanwise flow induced by the protuberances. As the amplitude of the protuberances is changed, the leading edge sweep angle is altered as well, which in turn modifies the strength of the streamwise vortices over the protuberances. As protuberance amplitude is increased, suction lift decreases whereas vortex lift increases. Because suction due to flow attachment is a more effective way of generating lift then vortices, the overall lift in the pre-stall regime will decrease with increasing protuberance amplitude. However, since the vortices become stronger with amplitude, lift in the post-stall regime will increase. This effectively creates a pay-off, with larger amplitude protuberances there is less lift due to flow attachment and more vortex lift, in turn generating low pre-stall lift but high post-stall lift. The opposite is true with smaller amplitude protuberances. In essence, load characteristics similar to the baseline foil show up as the baseline shape is approached.

The load measurements also show that the drag coefficients on all of the foils tested was nearly the same at post-stall angles of attack, while in the pre-stall regime drag was significantly higher. It is likely that at high angles of attack the drag coefficient has become so large that the foils become, essentially, bluff bodies. When this occurs the bumps have little effect on the drag of the foil. However, in the pre-stall regime, a larger amount of separation on foils with protuberances is apparent. The separation in turn generates higher drag coefficients at pre-stall angles of attack.

The measurements that have been reported here suggest applications of this work in an active flow control mechanism on control surfaces. The results show that it is not beneficial to use protuberances in the pre-stall regime because of the lift and drag penalties generated by the presence of protuberances. However, leading edge protuberances are useful in the post-stall regime generating significantly higher lift with little more drag than the baseline hydrofoil. Past work on finite wings yields significantly different results which show that the presences of protuberances on finite wings can be useful even if they are always present along the leading edge. Miklosovic's results[7] on finite wings show that it is possible to increase the performance of wings by adding protuberances to the leading edge with little or no penalty in either lift or drag.

5 Conclusions

The effects of leading edge protuberances on nominally two-dimensional NACA 63_4-021 airfoils were examined experimentally in a series of water tunnel tests. Two sets of hydrofoil models were fabricated: Set 1 had a span of 203 mm and was used to measure the forces and moments created by the foils and Set 2, having a span of 305 mm, was used to run flow visualization experiments to see qualitatively the flow patterns surrounding the hydrofoil surfaces. The amplitude of the leading edge of the protuberances ranged from 2.5% to 12% of the mean chord length, while the spanwise wavelength ranged from 25% to 50% of the mean chord length. The ranges of protuberance amplitude and wavelength correspond to those found on the leading edge of the humpback whale flipper. The lift, drag, and pitching moment coefficient were computed from the measured load data. The following conclusions can be drawn from the experiments.

The load measurements revealed difference in the lift, and drag coefficient characteristics between a foil with a straight, smooth leading edge and hydrofoils with protuberances. Measurements on the baseline foil revealed expected aerodynamic characteristics, whereas the foils with protuberances had quite different load characteristics. Most notably, the foils with protuberances did not separate and stall in the same manner as the baseline foil. At angles of attack in the pre-stall regime of the baseline foil, protuberances caused a reduction in lift. However, foils with protuberances generated as much as 50% more lift than the baseline foil in the post-stall regime of the baseline foil. Also, even though the baseline foil's lift coefficient dropped dramatically

after its stall angle, the lift coefficient of the foil with the largest amplitude protuberances generated a nearly constant lift coefficient for $10° \leq \alpha \leq 26°$.

In the pre-stall regime the foils with protuberances generated significantly higher drag; however, drag in the post-stall regime of the baseline was nearly independent of leading edge geometry. This indicates that in the post-stall regime the lift-to-drag ratio of the foils with protuberances can be increased substantially by using protuberances. In the post-stall regime it is possible to generate up to 50% higher lift than the baseline foil with relatively little or no drag penalty.

Two protuberance wavelengths were tested and the force measurements revealed that the wavelength of the protuberances played a minor role in the differences between force characteristics on foils with protuberances. Also, as shown in the experiment comparing the 8M and 8M* foils, the leading edge radius also plays a minor role in the lift and drag characteristics of the hydrofoils. The amplitude of the protuberances played a large role in creating a difference in the force and moment characteristics between the baseline hydrofoil and the hydrofoils with protuberances.

Flow visualization using tufts and dye were used to get qualitative insight on the flow patterns near the surface of the hydrofoils. Tuft visualization revealed that flow attachment ceases in the valleys located between two adjacent protuberances before the peaks of the protuberances. Also, there is a lack of flow attachment as compared to the baseline foil in the pre-stall angles of attack of the baseline foil, and this is most likely the major reason for lower lift coefficients and higher drag coefficients at pre-stall angles of attack. At the angle of attack where the baseline stalls, flow over the baseline is completely separated and reversed all the way to the leading edge of the foil. Foils with

protuberances, on the other hand, retain attachment on the peaks of the protuberances far beyond the stall angle of the baseline foil, thereby generating higher lift coefficients in the post-stall regime of the baseline foil.

Dye visualization at low Reynolds number revealed that on foils with protuberances, separation occurs first in the valleys of the protuberances while the flow over the peaks remains attached. Also, significant spanwise flow could be seen using dye, revealing asymmetry rather than the spanwise symmetry that is usually seen on 2-D hydrofoils. The spanwise flow between protuberances causes interactions between neighboring protuberances and generates a bi-periodic flow pattern along protuberances on the leading edge. At high angles of attack, neighboring valleys reveal one of two different flow patterns; 1) a general movement of flow away from the valley between two neighboring protuberances; or 2) a general movement of flow towards the valley. Each of these patterns extends to the neighboring peaks.

Finally, a pair of counter-rotating vortices stemming from the inflection points, seen in Figure 33, along the leading edge seems to help keep flow attached to the surface of the foils. These vortices contain similar characteristics to the vortices that appear on a delta wing. It is likely that that the vortices help keep flow attached along the peaks of the protuberances, hence generating more lift than the baseline foil, while simultaneously increasing the drag.

6 References

1 Fish, F. E. and Battle, J. M., "Hydrodynamic Design of the Humpback Whale Flipper," *Journal of Morphology*, Vol. 225, 1995, pp. 51-60.

2 Fish, F. E., "Performance Constraints on the Maneuverability of Flexible and Rigid Biological Systems," *Proceedings of the Eleventh International Symposium on Unmanned Untethered Submersible Technology (UUST)*, UUST99, Durham, New Hampshire, August 1999, pp. 394-406.

3 Bushnell, D. M. and Moore, K. J., "Drag Reduction in Nature," *Annual Review of Fluid Mechanics*, Vol. 23, January 1991, pp. 65-79.

4 Watts, P. and Fish, F. E., "The Influence of Passive, Leading Edge Tubercles on Wing Performance," *Proceedings of Unmanned Untethered Submersible Technology (UUST), UUST01*, Autonomous Undersea Systems Institute, Durham, New Hampshire, August 2001.

5 Miklosovic, D. S., Murray, M. M., Howle, L. E., and Fish, F. E., "Leading-edge Tubercles Delay Stall on Humpback Whale (Megaptera novaeangliae) Flippers," *Physics of Fluids*, Vol. 16, No. 5, May 2004, pp. L39-42.

6 Stein, B., Murray, M. M., "Stall Mechanism Analysis of Humpback Whale Flipper Models," *Proceedings of Unmanned Untethered Submersible Technology (UUST), UUST05*, Durham, New Hampshire, August 2005.

7 Murray, M. M., Miklosovic, D. S., Fish, F. E., and Howle, L., "Effects of Leading Edge Tubercles on a Representative Whale Flipper Model at Various Sweep Angles," *Proceedings of Unmanned Untethered Submersible Technology (UUST), UUST05, Durham*, New Hampshire, August 2005.

8 Bearman, P. W. and Owen, J. C., "Reduction of Bluff-Body Drag and Suppression of Vortex Shedding by the Introduction of Wavy Separation Lines," *Journal of Fluids and Structures*, Vol. 12, 1998, pp. 123-130.

9 Bearman, P. W. and Tombazis, N., "The Effect of Three-Dimensional Imposed Disturbances on Bluff Body Near Wake Flows," *Journal of Wind Engineering and Industrial Aerodynamics*, Vol. 49, 1993, pp. 339-350.

10 Naumann, A., Morsbach, M., and Kramer, C., "The Conditions of Separation and Vortex Formation Past Cylinders*," AGARD conference proceedings no. 4, Separated Flows*, 1966, pp. 539-574.

11 Owen, J. C. and Bearman, P. W., "Passive Control of VIV with Drag Reduction," *Journal of Fluids and Structures*, Vol. 15, 2001, pp. 597-605.

12 Tanner, M., “A Method of Reducing the Base Drag of Wings with Blunt Trailing Edges,” *Aeronautical Quarterly*, Vol. 23, 1972, pp. 15-23.

13 Tombazis, N. and Bearman, P. W., “A study of Three-Dimensional Aspects of Vortex Shedding from a Bluff Body with a Mild Geometric Disturbances,” *Journal of Fluid Mechanics*, Vol. 330, 1997, pp. 85-112.

14 Gad-el-Hak, M. and Bushnell, D.M., “Separation Control: Review,” *Journal of Fluids Engineering*, Vol. 113, 1991, pp. 5-30.

15 Pope, A. and Ray, W.H., "Low-speed Wind Tunnel Testing," 2nd edition, Wiley, New York, 1984.

16 Coleman, H. and Steel, W., "Experimentation and Uncertainty Analysis for Engineers," Wiley-Interscience, 1989.

17 Abbott, I.H., and Von Doenhoff, A.E., "Theory of Wing Sections," Dover, New York, 1959.

18 Cebeci, T., Clark, R.W., Chang, K.C., Halsey, N.D. and Lee, K., “Airfoils with Separation and the Resulting Wakes,” *Journal of Fluid Mechanics*, Vol. 163, 1986, pp.323-347.

19 Hoarau, Y., Braza, M. Ventikos, Y., Faghani, D., and Tzabiras, G., “Organized Modes and Three-dimensional Transition to Turbulence in the Incompressible flow around a NACA0012 Wing,” *Journal of Fluid Mechanics,* Vol. 496, September 2003, pp. 63-72.

20 Johari, H., Henoch, C., Custodio, D. and Levshin., A., “Effects of Leading-Edge Protuberances on Airfoil Performance,” *AIAA Journal*, Vol. 45, No. 11, November 2007, pp. 2634-2642.

21 Miklosovic, D. S., Murray, M. M., and Howle, L. E, “Experimental Evaluation of Sinusoidal Leading Edges,” *Journal of Aircraft; Engineering Notes*, Vol. 44, No. 4, July-August 2007, pp. 1404-1407.

22 Sunada, S., Sakaguchi, A., and Kawachi, K., “Airfoil Section Characteristics at a Low Reynolds Number,” *Journal of Fluids Engineering,* Vol. 119, March 1997, pp. 129-135.